



A robust well-balanced model on unstructured grids for shallow water flows with wetting and drying over complex topography



Jingming Hou ^{*}, Franz Simons, Mohamed Mahgoub, Reinhard Hinkelmann

Chair of Water Resources Management and Modeling of Hydrosystems, Department of Civil Engineering, Technische Universität Berlin, TIB 1-B14, Gustav-Meyer-Allee 25, 13355 Berlin, Germany

ARTICLE INFO

Article history:

Received 17 May 2012

Received in revised form 4 November 2012

Accepted 21 January 2013

Available online 13 February 2013

Keywords:

Shallow water equations (SWEs)

Unstructured grids

Cell-centered finite volume method

Well-balanced scheme

Wet-dry fronts

Uneven bed

ABSTRACT

To simulate complex flows involving wet-dry fronts in irregular terrains over arbitrary beds, this paper presents a 2D well-balanced shallow water flow model, based on an unstructured cell-centered finite volume scheme. In this model, hydrostatic reconstruction is applied to reconstruct non-negative water depths at wet-dry interfaces. Harten, Lax and van Leer approximate Riemann solver with the contact wave restored is employed to compute the fluxes of mass and momentum. In addition, the splitting point-implicit method is utilized to solve the friction source terms. The novel aspects of the model include the adaptive method and the slope source term treatment. The former is devised to prevent unphysical high velocities occurring in the part of the domain with varying thin water and topography. The latter converts the slope source terms of a cell into fluxes through its edges and takes account of the influence of wet-dry fronts, so as to satisfy the C-property in any case on unstructured grids. The accuracy and robustness of the proposed model are extensively verified against several benchmark tests as well as a real dam-break event, where its superiority in simulating complex flows with wetting and drying over uneven bed is emphasized.

© 2013 Elsevier B.V. All rights reserved.

1. Introduction

A shallow water flow model, which acts as a mathematical tool to solve shallow water equations (SWEs), plays a significant role in simulating hydrodynamics in a wide variety of surface flows, e.g. water flows in rivers, channels, flood plains, estuaries and coastal regions. Being a good shallow water flow model, accuracy, robustness and efficiency are all indispensable. However, it is not easy to achieve all of them at the same time, especially on complex unstructured grids, which can be made to conform to nearly any desired geometry. Therefore, the research on seeking a satisfactory numerical solution to SWEs on unstructured grids seems remarkably promising.

In recent decades, Godunov-type schemes within the cell-centered finite volume framework became popular in solving SWEs numerically [1–35]. Using Godunov-type scheme, most complicated shallow water flow phenomena such as transcritical flows, shock-type flows and moving wet-dry interface of a water wave front can be appropriately simulated [5]. However, on unstructured grids, challenges still exist to achieve second order accuracy,

to preserve the well-balanced property [36] or C-property [37], and to handle wetting and drying over complex topography.

To extend a model for 2D unstructured grids to be in second order accuracy without unphysical oscillations, Runge–Kutta scheme is generally used to achieve second order temporal accuracy [38,3,39,14,18,15,40,41], and monotone upstream scheme for conservation law (MUSCL) technique [42] is widely used to reconstruct the values of variables in space [38,10–12,14,15,43,3,44,41,45,35], on unstructured grids.

In addition to the second order accuracy, a good shallow water flow model should also satisfy the well-balanced properties [36]. That is, a steady solution is maintained by treating the slope source terms reasonably according to the fluxes. Generally speaking, a scheme can be regarded as well-balanced scheme if it satisfies the C-property of [37], i.e. quiescent states are preserved [46,47,17,39,18,19,5,6,14,15,44,32,26,48,49,45,50–52,35].

With the upwind discretization method [53,39,18], the numerical fluxes balance the bed slope source terms well for first order schemes in wet cells, but corrections are required for second order MUSCL discretizations [53,54,39,18], so a special treatment for wet-dry fronts. Begnudelli and Sanders [10] introduced a flux correction method to maintain the well-balanced properties in fully wet cells, but unphysical high velocities may occur near wet-dry fronts. To release this problem Song et al. [14] developed a new flux correction for both fully and partially submerged cells. However, it may lead to another problem of momentum non-conserva-

* Corresponding author.

E-mail addresses: jingming.hou@wahyd.tu-berlin.de (J. Hou), franz.simons@wahyd.tu-berlin.de (F. Simons), mohamed.mahgoub@wahyd.tu-berlin.de (M. Mahgoub), reinhard.hinkelmann@wahyd.tu-berlin.de (R. Hinkelmann).

tion in unsteady situations, since the flux corrections may be unequal on both sides of an edge. Another correction method was suggested by Benkhaldoun et al. [44,32] to correct the water depth in the slope source terms. But it is not able to cope with the occurrence of wet-dry fronts. Liang and Borthwick [4] proposed pre-balanced SWEs to treat the slope source terms with the water level instead of the water depth. Thus no additional corrections are needed for wet cells. However, an additional reconstruction for Riemann states is necessary at wet-dry fronts. Song et al. [15] applied the pre-balanced SWEs on unstructured grids by using a slope bottom model together with volume-free surface relationships (VFRs in [10]) in partially submerged cells. VFRs are expensive due to a complex process to compute the free surface, especially in partially submerged cells. The well-balanced properties in hydrostatic reconstruction method are preserved by an interface hydrostatic reconstruction for the values and a different slope source term treatment, with which the slope source in a cell is transformed into fluxes at its edges [46,47]. Hence, it is quite adaptive to unstructured grids and no additional correction is demanded for wet-dry fronts. A similar method which also converts the slope source into fluxes is developed in [35]. This method incorporated with the proposed non-negative water depth reconstruction, the C-property is well preserved.

For wetting and drying of the bed surface, challenges are to get rid of numerical instabilities, which result for example in unphysical high velocities or negative water depths, and in turn in non-conservation of mass. Hence, numerical methods for wetting and drying are a topic of active research in the last decade.

Bradford and Sanders [8] varied the free surface reconstruction scheme and updated the velocities with Neumann extrapolation near wet-dry interfaces, so as to prevent spurious wave generation. Brufau et al. [55] presented a strategy to control numerical instabilities, by means of a wetting-drying condition for both steady and unsteady shallow water flows, together with a local redefinition of the bed slope. Both [8,55] reported that during wave recession, overdraft of cells might occur, and thus adopted a correction step to compensate for the overdrafted water from neighboring wet cells. Castro et al. [56] improved the technique in [54] to treat a wet-dry interface like an internal boundary. This technique was also employed in [57,17,39,18] to model wetting and drying. Sometimes the slope is very steep and drying the slope with this technique leads to negative depth in the drying cell, thus, the aforementioned correction step is incorporated to prevent instability [39,18]. Murillo et al. [28] developed a stability condition linked to the variations of bed and flow. However, drying processes may lead to strong restrictions in the magnitude of the time step and unacceptable computational costs. In order to avoid the necessity of reducing the time step [28] also introduced a technique to apply the largest possible time step compatible with stability. Begnudelli and Sanders [10,11] presented VFRs to cope with wetting and drying, in conjunction with a modified flux computation. Based on VFRs [15] developed a slope bottom model to track wet-dry fronts. But the mass conservation is not well preserved, because the negative water depths predicted are set to zero. Unlike most of the aforementioned methods which require a wet-dry tolerance or threshold ε_{wd} , e.g., $\varepsilon_{wd} = 1 \times 10^{-6}$ m [55,10,11,34,35], $\varepsilon_{wd} = 1 \times 10^{-10}$ m [5–7] or a case-dependent ε_{wd} in [58,18], Casulli [59] developed a new method which did not require any wet-dry tolerance. In this method, wet-dry fronts are tracked by solving an additional non-linear system. Zokagoa and Soulard [34] proposed a free surface correction (FSC) at wet-dry interfaces, so as to avoid spurious numerical oscillations for water fronts advancing over adverse steep slope. The aforementioned hydrostatic reconstruction method [46,47] also does well in modeling wet-dry fronts in motion, by means of an interface non-negative water depth reconstruction. Due to a concise algorithm and satisfactory performance,

this method is incorporated in the models of [60,4–7] to treat wet-dry fronts.

The velocities at the midpoint of the considered edge e (Fig. 2), which are used to compute fluxes, are usually evaluated by

$$u_M = q_{xM}/h_M, \quad v_M = q_{yM}/h_M, \quad (1)$$

where, q_x and q_y are the components of per unit width discharge; h denotes the water depth and the subscript M denotes the midpoint of the edge e . For first order schemes, u_M and v_M are equivalent to those at the corresponding cell centroid, therefore, no local extreme values occur. For second order schemes, q_{xM} , q_{yM} and h_M are extrapolated with for example the MUSCL schemes. In this case, the computed u_M and v_M by Eq. (1) from the extrapolated q_{xM} , q_{yM} and h_M may be the local extreme values, especially in the area with varying thin water and topography (sensitive part in Fig. 1), even though q_x , q_y and h are monotonic. These local extreme values of u_M and v_M may be quite unrealistic and thus lead to erroneous fluxes and in turn to numerical problems, e.g. negative water depths and unphysical high velocities at cell centroids. Moreover, unphysical high velocities will reduce the time step when the CFL condition is used to maintain numerical stability.

This problem can be circumvented by using primitive variables (PVs) (u, v) directly, rather than conservative variables (CVs) (q_x, q_y) as that in [61], however, the use of PVs yields more energy loss in subcritical flow. Consequently, an adaptive approach was devised by Begnudelli et al. [12] to change the variables with the local Froude number F , i.e. PVs were adopted when $F > 1$. But it can not solve this problem thoroughly, since subcritical flow may still exist in the sensitive part, where unreasonable u_M and v_M may occur. A new formula was introduced in [62] to alleviate this problem and reads as

$$u_M = \frac{\sqrt{2}h_M q_{xM}}{\sqrt{h_M^4 + \max(h_M^4, \varepsilon)}}, \quad v_M = \frac{\sqrt{2}h_M q_{yM}}{\sqrt{h_M^4 + \max(h_M^4, \varepsilon)}}, \quad (2)$$

where, ε is a prescribed tolerance and $\varepsilon = (\Delta x)^4$ in [62] and $\varepsilon = T^2$ (T is the maximum area of cell) in [63]. If h_M is lower than the cell size or an equivalent one, u_M and v_M are modified by Eq. (2), thus the possible unphysical high velocities can be avoided. However, as u_M and v_M are also modified for some cases, where $h_M < \Delta x$, u_M and v_M computed with Eq. (1) are not unphysical high values, this method may produce unsatisfactory results. For example, in a case with shallow uniform flow whose water depth is smaller than the sizes of all cells, the velocities must be modified in all cells when using this method. Thus the flow is wrongly computed.

As first order schemes won't cause unphysical high u_M and v_M , this problem can also be solved by switching locally second order schemes to first order ones [14,15,28,23,29,30]. Song et al. [14] set the values of variables at M to be identical to those at cell centroids,

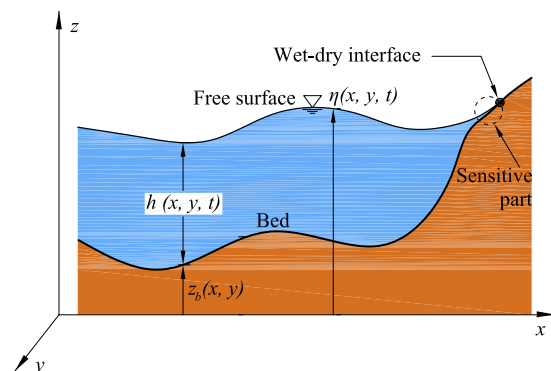


Fig. 1. Sketch of free-surface flow with wet-dry interface and notations of some variables.

under the condition that h_M is lower than a small positive value $\delta_h = 0.1$ m. This condition was modified to be that u_M or v_M is higher than $\delta_v = 30$ m/s in [15]. Obviously, either δ_h or δ_v is quite case-dependent. Liang [6] suggested a similar adaptive approach according to the wet-dry conditions, i.e. the edge values were extrapolated with second order scheme in those wet cells away from the wet-dry interface, while they were assumed to be identical to those at the cell centroids in a dry or wet cell next to a dry cell. However, when this approach is used to simulate wet-dry fronts moving over strongly varying bed, especially on complex unstructured grids, unphysical high velocities may still be produced with Eq. (1), at some interfaces between cells with varying small water depths and varying bed elevations (sensitive part in Fig. 1). In the cases where water depths vary drastically or source terms dominate over fluxes, the second order scheme in [23,29,30] is reduced to first order. This method is able to cure numerical instabilities caused by second order scheme. However, in the area with varying water depth which may not cause unphysical high velocities, e.g. the shock front of a dam break wave over a flat wet bed, loss of accuracy may occur.

To simulate complex shallow water flows involving wetting and drying in complex terrains over complex beds, this work develops a robust and efficient 2D well-balanced shallow water flow model on unstructured grids, within the framework of Godunov-type cell-centered finite volume scheme. The MUSCL scheme of [64] is applied to extrapolate the values at the midpoint M of the considered edge. These values are then modified by the hydrostatic reconstruction [46,47], with which, non-negative water depth at each interface can be maintained. The modified values are used to compute the fluxes of mass and momentum and to evaluate the slope source terms. The Harten, Lax, and van Leer approximate Riemann solver with the contact wave restored (HLLC) developed by Toro et al. [65] is utilized to compute the fluxes. A slope source term treatment is proposed to preserve the C-property for any case on arbitrary grids. The splitting point-implicit method described in [5] is employed to calculate the friction source terms. Moreover, in order to avoid unphysical high velocities caused by MUSCL reconstruction for varying thin flow over varying bed, an adaptive method is devised.

This paper is organized as following: governing equations and numerical methods are presented in Section 2. Then the model is verified against some theoretical and experimental benchmark tests and a real dam-break case in Section 3. Finally, the conclusions are drawn in Section 4.

2. Governing equations and numerical methods

2.1. Shallow water equations

The 2D shallow water equations have different forms such as the pre-balanced SWEs in [5,4,6,7] and the classical conservative SWEs in [14,15]. If the kinetic and turbulent viscous terms, wind stresses and Coriolis effects are neglected, the latter, which are used as governing equations in this work, are given by

$$\frac{\partial \mathbf{q}}{\partial t} + \frac{\partial \mathbf{f}}{\partial x} + \frac{\partial \mathbf{g}}{\partial y} = \mathbf{S}, \quad (3)$$

$$\mathbf{q} = \begin{bmatrix} h \\ q_x \\ q_y \end{bmatrix},$$

$$\mathbf{f} = \begin{bmatrix} q_x \\ uq_x + gh^2/2 \\ uq_y \end{bmatrix}, \quad \mathbf{g} = \begin{bmatrix} q_y \\ vq_x \\ vq_y + gh^2/2 \end{bmatrix},$$

$$\mathbf{S} = \mathbf{S}_b + \mathbf{S}_f = \begin{bmatrix} 0 \\ -gh\partial z_b/\partial x \\ -gh\partial z_b/\partial y \end{bmatrix} + \begin{bmatrix} 0 \\ -C_f u \sqrt{u^2 + v^2} \\ -C_f v \sqrt{u^2 + v^2} \end{bmatrix}, \quad (4)$$

where, t is the time; x and y are the Cartesian coordinates; \mathbf{q} represents the flow variable vector consisting of h , q_x and q_y , which denote water depth, unit-width discharges in x - and y -direction, respectively; u , v are defined as depth-averaged velocities in x - and y -direction and clearly $q_x = uh$ and $q_y = vh$; \mathbf{f} and \mathbf{g} are the flux vectors in x - and y -direction; \mathbf{S} is the source vector only considering the slope source \mathbf{S}_b and the friction source \mathbf{S}_f , herein z_b is the bed elevation and C_f is the bed roughness coefficient determined by the Manning coefficient n and h in the form of $gn^2/h^{1/3}$. In addition, the water level η which equals to $h + z_b$ is also used in this work.

2.2. Finite volume discretization for SWEs on unstructured grids

Using cell-centered finite volume method, an integral form of Eq. (3) over a control cell is written as

$$\int_{\Omega} \frac{\partial \mathbf{q}}{\partial t} d\Omega + \int_{\Omega} \left(\frac{\partial \mathbf{f}}{\partial x} + \frac{\partial \mathbf{g}}{\partial y} \right) d\Omega = \int_{\Omega} \mathbf{S} d\Omega, \quad (5)$$

where, Ω is the volume of the control cell i . Applying divergence theorem, Eq. (5) becomes

$$\int_{\Omega} \frac{\partial \mathbf{q}}{\partial t} d\Omega + \oint_{\Gamma} \mathbf{F}(\mathbf{q}) \cdot \mathbf{n} d\Gamma = \int_{\Omega} (\mathbf{S}_b + \mathbf{S}_f) d\Omega, \quad (6)$$

in which, Γ is the boundary of the control cell; \mathbf{n} denotes the unit outward vector normal to the considered boundary and is defined by $(n_x, n_y)^T$; $\mathbf{F}(\mathbf{q}) \cdot \mathbf{n}$ is the flux vector normal to the boundary and is expressed as

$$\mathbf{F}(\mathbf{q}) \cdot \mathbf{n} = (\mathbf{f} \mathbf{n}_x + \mathbf{g} \mathbf{n}_y) = \begin{bmatrix} q_x n_x + q_y n_y \\ (uq_x + gh^2/2)n_x + vq_x n_y \\ uq_y n_x + (vq_y + gh^2/2)n_y \end{bmatrix}. \quad (7)$$

The line integral for $\mathbf{F}(\mathbf{q}) \cdot \mathbf{n}$ over all edges of a triangular cell can be rewritten into an algebraic form as

$$\oint_{\Gamma} \mathbf{F}(\mathbf{q}) \cdot \mathbf{n} d\Gamma = \sum_{k=1}^3 \mathbf{F}_k(\mathbf{q}) \cdot \mathbf{n}_k l_k, \quad (8)$$

where, k and l are the index and length of the edge of cell i , respectively.

2.3. Time integration

A second order temporal accuracy can be obtained by applying the two-stage explicit Runge–Kutta scheme [38,4,5,14,6,7,15], \mathbf{q}_i^{n+1} of cell i in the new time step is updated by

$$\mathbf{q}_i^{n+1} = \frac{1}{2} [(\mathbf{q}_i^n + \mathbf{q}_i^{n*}) + K(\mathbf{q}_i^{n*})], \quad (9)$$

where

$$\mathbf{q}_i^{n*} = \mathbf{q}_i^n + \mathbf{K}(\mathbf{q}_i^n), \quad (10)$$

and $\mathbf{K}(\mathbf{q}_i^n)$ is computed from

$$\mathbf{K}(\mathbf{q}_i^n) = \frac{\Delta t^n}{\Omega} \left[\int_{\Omega} \mathbf{S}(\mathbf{q}^n) d\Omega - \sum_{k=1}^3 \mathbf{F}_k(\mathbf{q}^n) \cdot \mathbf{n}_k l_k \right]. \quad (11)$$

2.4. MUSCL reconstruction

If the values of \mathbf{q} are assumed as constant within each cell, only first order spatial accuracy is achieved. In order to increase spatial accuracy and to avoid overshoots and undershoots on 2D

unstructured grids, MUSCL-type slope limiting methods are widely used to reconstruct the linear gradient in each cell [38,3,39,14,18,15,40,41]. This kind of methods are referred to as cell-based limiting methods and are different from edge-based limiting methods which reconstruct the values of variables at each edge of a cell [35,19]. In contrast to the latter, the former can provide piecewise linear gradients for cells and give a monotonic linear function on each cell which can preserve the mean values in the cell. The cell-based limiting method proposed by Venkatakrishnan [64], whose limiter is differentiable and performs well for both steady and dynamic cases [66,67], is adopted in this work. It consists of two steps. First, a predicted or unlimited gradient is computed for each cell of the mesh using neighboring values. Second, the unlimited gradient is limited by an appropriate limiter to maintain the monotonicity.

For a component q of the variable vector \mathbf{q} , the unlimited gradient $\nabla \bar{q}_i$ at the i th triangular cell is based on its values q_{j_1}, q_{j_2} and q_{j_3} at three adjacent points, $(x_{j_1}, y_{j_1}), (x_{j_2}, y_{j_2})$ and (x_{j_3}, y_{j_3}) , respectively [10]

$$\nabla \bar{q}_i = \mathbf{J} \begin{pmatrix} q_{j_2} - q_{j_1} \\ q_{j_3} - q_{j_1} \end{pmatrix}, \quad (12)$$

$$\mathbf{J} = \frac{1}{(x_{j_2} - x_{j_1})(y_{j_3} - y_{j_1}) - (x_{j_3} - x_{j_1})(y_{j_2} - y_{j_1})} \begin{pmatrix} y_{j_3} - y_{j_1} & y_{j_1} - y_{j_2} \\ x_{j_1} - x_{j_3} & x_{j_2} - x_{j_1} \end{pmatrix}. \quad (13)$$

The three points can be three nodes of the considered cell or the centroids of the three surrounding cells, the latter are chosen in this work, because they are fit for the cell-centered finite volume method (Fig. 2(a)).

The limited gradient of the variable q at the i th cell is then obtained by limiting the unlimited gradient as

$$\nabla q_i = \Phi_i \nabla \bar{q}_i, \quad (14)$$

where Φ denotes the limiting function and is given by

$$\Phi_i = \min_{k=1,2,3} (\Phi_{ik}), \quad (15)$$

$$\Phi_{ik} = \begin{cases} \Phi\left(\frac{q_i^{\max} - q_i}{q_{M_k}^L - q_i}\right) & \text{if } \bar{q}_{M_k}^L - q_i > 0, \\ \Phi\left(\frac{q_i^{\min} - q_i}{q_{M_k}^R - q_i}\right) & \text{if } \bar{q}_{M_k}^R - q_i < 0, \\ 1 & \text{if } \bar{q}_{M_k}^L - q_i = 0, \end{cases} \quad (16)$$

in which, q_i is the value at the centroid of the i th cell; $q_i^{\max} = \max(q_i, q_{j_1}, q_{j_2}, q_{j_3})$ and $q_i^{\min} = \min(q_i, q_{j_1}, q_{j_2}, q_{j_3})$; the subscript M_k denotes the midpoint of the k th edge; $\bar{q}_{M_k}^L$ is the value at M_k extrapolated by the unlimited gradient and is obtained by

$$\bar{q}_{M_k}^L = q_i + \nabla \bar{q}_i \cdot \mathbf{r}_{i,M_k}, \quad (17)$$

herein, \mathbf{r} is the position vector relative to the centroid of the cell. For the case with $\bar{q}_{M_k}^L - q_i > 0$ or $\bar{q}_{M_k}^L - q_i < 0$, letting $\Delta_- = \bar{q}_{M_k}^L - q_i$, $\Delta_+ = q_i^{\max} - q_i$ if $\bar{q}_{M_k}^L - q_i > 0$, or $\Delta_+ = q_i^{\min} - q_i$ if $\bar{q}_{M_k}^L - q_i < 0$,

$$\Phi_{ik} = \Phi\left(\frac{\Delta_+}{\Delta_-}\right) = \frac{1}{\Delta_-} \left[\frac{(\Delta_+ + \varepsilon^2)\Delta_- + 2\Delta_-^2\Delta_+}{\Delta_+^2 + 2\Delta_-^2 + \Delta_-\Delta_+ + \varepsilon^2} \right]. \quad (18)$$

In this equation, $\varepsilon^2 = (K\Delta x)^3$ and is used to improve the convergence in uniform region [64]. However, since for any $K > 0$ the limiter no longer strictly enforces monotonicity, large values of K can lead to significant overshoots near discontinuities in solutions [66]. As the main purpose of this work is to construct a robust model to simulate complex flow involving wetting and drying, K is taken to be zero to ensure the robustness. Thus, Eq. (18) can be simplified as

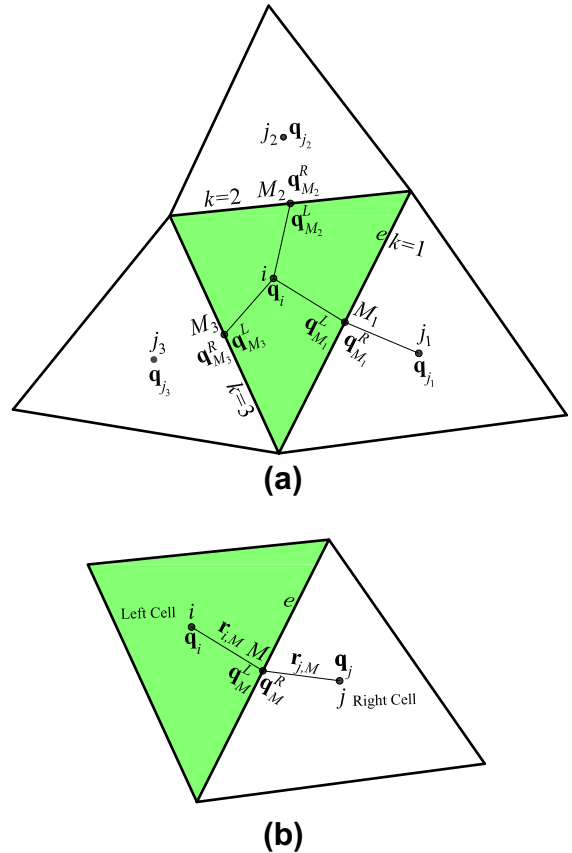


Fig. 2. Variable's notation on a triangular grid: (a) for the i th cell, (b) for the considered edge e ($k = 1$).

$$\Phi(y) = \frac{y^2 + 2y}{y^2 + y + 2}. \quad (19)$$

It should be noted, if the considered cell has one edge at the boundary as sketched in Fig. 3(a), the three points used to estimate the gradients are the centroid and the two neighboring centroids inside the computational domain [10,44,33]. If the cell has only one neighboring inner cell, ∇q_i is assumed equal to $(0, 0)^T$, i.e. $q_{M_k}^L = q_i$ (Fig. 3(b)).

With the limited gradient computed by Eq. (14), the left and right states of the variables at the midpoint of the k th edge can be extrapolated by

$$\begin{aligned} \mathbf{q}_{M_k}^L &= \mathbf{q}_i + \nabla \bar{q}_i \cdot \mathbf{r}_{i,M_k}, \\ \mathbf{q}_{M_k}^R &= \mathbf{q}_{j_k} + \nabla \bar{q}_{j_k} \cdot \mathbf{r}_{j_k,M_k}. \end{aligned} \quad (20)$$

At the considered edge e , $\mathbf{q}_{M_k}^L$ and $\mathbf{q}_{M_k}^R$ are written as \mathbf{q}_M^L and \mathbf{q}_M^R for the sake of simplicity (Fig. 2(b)). As proposed in [46,47,4–7], only η, h, q_x and q_y are extrapolated to be $\eta_M^L, \eta_M^R, h_M^L, h_M^R, q_{xM}^L, q_{xM}^R, q_{yM}^L$ and q_{yM}^R , respectively, at the midpoint M with Eq. (20). The bed elevations z_{bM}^L and z_{bM}^R are computed from

$$z_{bM}^L = \eta_M^L - h_M^L, \quad z_{bM}^R = \eta_M^R - h_M^R. \quad (21)$$

Additionally, velocities at M are calculated by

$$\begin{aligned} v_M^L &= q_{xM}^L/h_M^L, & v_M^L &= q_{yM}^L/h_M^L, \\ v_M^R &= q_{xM}^R/h_M^R, & v_M^R &= q_{yM}^R/h_M^R. \end{aligned} \quad (22)$$

2.5. Adaptive method maintaining numerical stability

At some interfaces between cells with varying small water depths and varying bed elevations, e.g. those adjacent to the

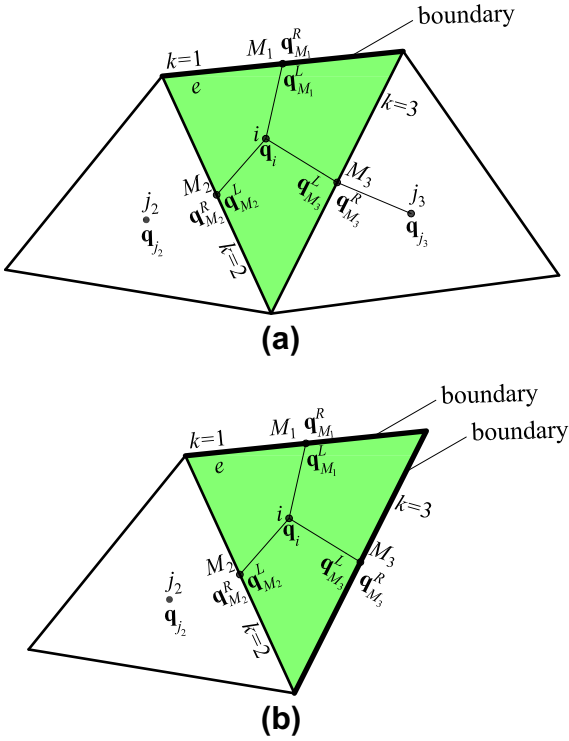


Fig. 3. Variable's notation on a triangular grid: (a) for the i th cell with one edge at the boundary, (b) for the i th cell with two edges at the boundary.

wet-dry interface or in its vicinity (sensitive part in Fig. 1), second order scheme (Eq. (20)) may produce unphysical high velocities by Eq. (22), especially on complex unstructured grids. For instance, $|u_M| \gg \max(|u_M^{\min}|, |u_M^{\max}|)$ may appear. When these unphysical high velocities are used to compute the fluxes, they may lead in turn to physically meaningless predictions of flow variables at cell

centroids, such as negative water depths and unphysical high velocities. For example, if the MUSCL reconstruction is imposed in all cells, the present model will give rise to numerical instabilities near wet-dry fronts, for the test case of Thacker's planar solution [68], even though a stability criterion of [18,19] is adopted, see Fig. 4. The stability criterion defined in [28,23,29,30], which constrains the time step at edge, is able to prevent negative water depths caused by unphysical high velocities. However, it may result in a strong restriction in the magnitude of the time step, and thus, the computational cost is quite unacceptable.

The unphysical high velocities computed with Eq. (22) can be avoided successfully by using the first order scheme. Therefore, to impose the first order scheme locally in the sensitive cells, where the MUSCL reconstruction may lead to unphysical high velocities, becomes a popular method as mentioned in the introduction [6,35,28,23,29,30,14,15]. Based on this ideal, a new method is developed in this work to determine such sensitive cells.

The immediate cause of the unphysical high velocities at M lies in the discharges being divided by a very small water depth, which is evaluated by the MUSCL reconstruction. From this point of view, if such small water depth extrapolated at M of any edge of the considered cell is predicted, this problem will be alleviated by using the first order scheme in this cell. As illustrated in Fig. 5, for MUSCL reconstruction, the very small h_M^L can be predicted by \bar{h}_M^L , which is the water depth at M computed by the unlimited gradient (Eq. (17)). \bar{h}_M^L is likely to be negative in the sensitive area involving varying small water depth and varying topography (Fig. 5(a)). If this is the case, \bar{h}_M^L will be reconstructed to h_M^L by the limited gradient of water depth with Eq. (17). The value of h_M^L may be very small and close to that of h_i^{\min} (Fig. 5(a)), so unphysical high velocities are prone to occur. According to this, the cells where $\bar{h}_{M_k}^L < 0$ at any k edge are defined as sensitive cells, in which the first order scheme is imposed locally for all variables. Moreover, for dry cells which are identified by their water depths are lower than a tolerance ε_{wd} ($\varepsilon_{wd} = 10^{-6}$ m in this work), to preserve the stability and to increase efficiency, first order scheme is also imposed locally. For the considered cell i , this method can be summarized as

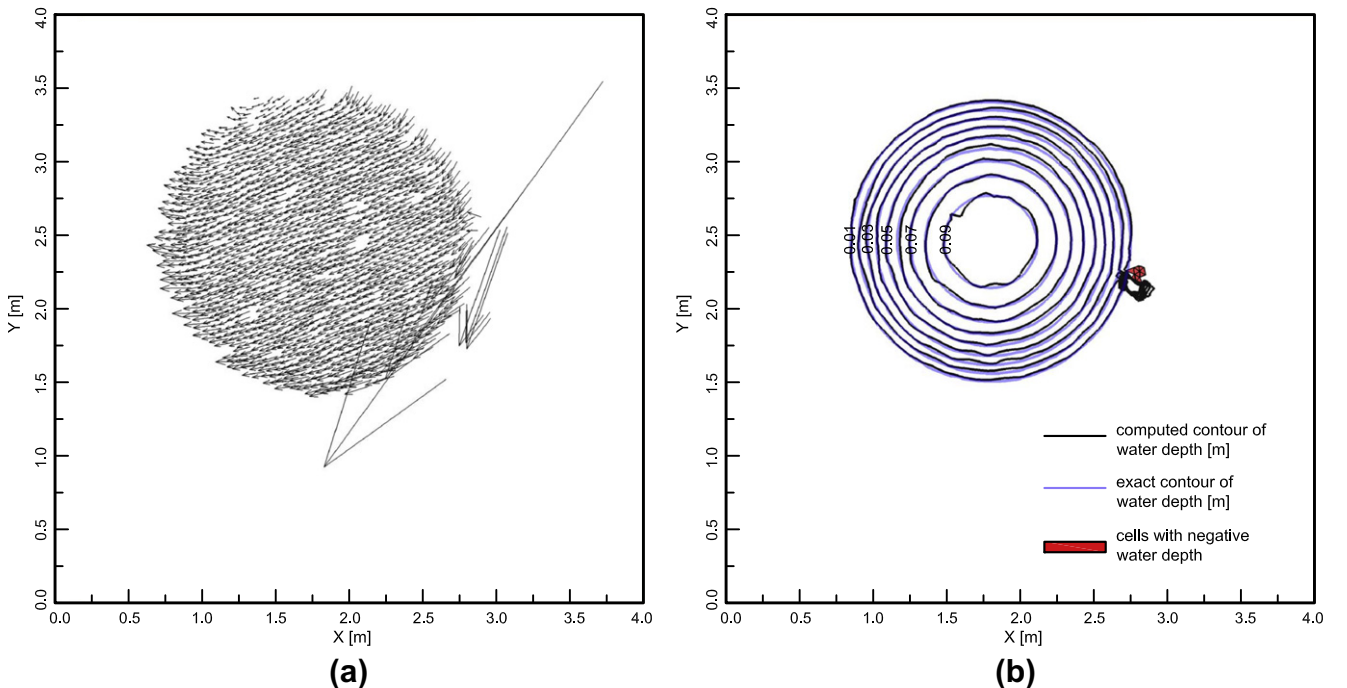


Fig. 4. Unrealistic computed values of flow variables for the Thacker's planar solution [68] at $t = 5.9$ s: (a) unphysical high velocities, (b) negative water depths.

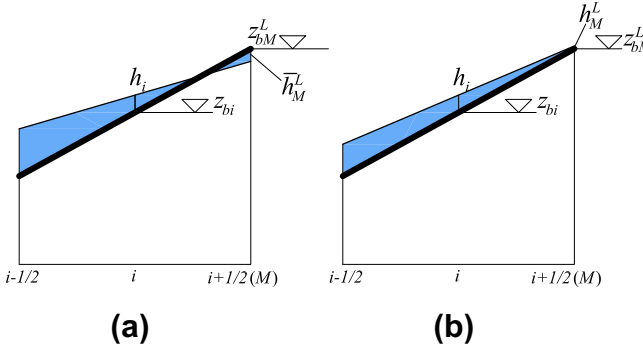


Fig. 5. MUSCL reconstruction for the water depth at a cell with varying small water depth and varying bed elevation: (a) the value at M extrapolated by the unlimited gradient, (b) the value at M extrapolated by the limited gradient.

if $(h_i \leq \varepsilon_{wd} \text{ or } \bar{h}_{M_k}^L < 0)$

$$\text{First order scheme : } \mathbf{q}_{\mathbf{M}_k}^L = \mathbf{q}_i; \quad (23)$$

else

$$\text{Second order scheme : } \mathbf{q}_{\mathbf{M}_k}^L = \mathbf{q}_i + \nabla \mathbf{q}_i \cdot \mathbf{r}_{i,M_k}.$$

The proposed method is termed as adaptive method and it owns the following features:

- It is able to prevent unphysical high velocities induced by the MUSCL reconstruction and some consequent numerical instabilities or strong restriction of the time step. Therefore it renders the model more robust and efficient in simulating wetting and drying over complex topography on unstructured grids. For example, unphysical high velocities and negative water depths sketched in Fig. 4 can be avoided by this adaptive method, as demonstrated in Fig. 18.
- The sensitive cells are determined by $\bar{h}_{M_k}^L < 0$ at any edge of a cell, so the method is not case-dependent and thus more versatile for practical applications.
- When simulating wetting and drying, the application of the first order scheme in the sensitive cells and the dry cells can make the model more efficient, since the first order scheme does not need any expensive algorithm such as the computations of gradients for irregular cells.

In addition, as $\varepsilon_{wd} = 1 \times 10^{-6}$ m is used to identify the dry cells as that in [55,10,11,34], the sensitivity of different values of ε_{wd} will be investigated in Section 3.4.

2.6. Hydrostatic reconstruction

In a case involving wet-dry fronts, a proper modification for the variables at wet-dry interfaces is necessary to preserve non-negative water depths and the C-property of [37]. For this purpose Audusse et al. [46] proposed a robust positivity preserving method to modify the variables at cell interfaces, and a good performance was witnessed in [47,60,4–7]. The hydrostatic reconstruction for edge values can be carried out in the following steps. Firstly, the bed elevation at the midpoint of the considered edge is expressed by

$$z_{bM} = \max(z_{bM}^L, z_{bM}^R). \quad (24)$$

Secondly, the non-negative \mathbf{h}_M^L and \mathbf{h}_M^R are modified as

$$h_M^L = \max(0, \eta_M^L - z_{bM}), \quad (25)$$

$$h_M^R = \max(0, \eta_M^R - z_{bM}). \quad (25)$$

Finally, according to Eq. (25) the modified discharges on both sides of edge e are obtained as

$$\begin{aligned} q_{xM}^L &= h_M^L u_M^L, & q_{yM}^L &= h_M^L v_M^L, \\ q_{xM}^R &= h_M^R u_M^R, & q_{yM}^R &= h_M^R v_M^R, \end{aligned} \quad (26)$$

where, u_M^L, v_M^L, u_M^R and v_M^R are evaluated with Eq. (22). $z_{bM}, h_M^L, h_M^R, q_{xM}^L, q_{yM}^L, q_{xM}^R$ and q_{yM}^R obtained with Eqs. (24)–(26) will be employed to compute the fluxes and the slope source terms.

2.7. Interface flux calculation

As an approximate Riemann solver which suits the cases involving wet-dry interfaces, the HLLC approximate Riemann solver developed by Toro et al. [65] and implemented successfully in [5,4,6,14,15,7,35], is adopted here to calculate the fluxes through the considered edge e ($\mathbf{F}_k(\mathbf{q}) \cdot \mathbf{n}_k$ in Eq. (8)). By applying \mathbf{q}_M^L and \mathbf{q}_M^R which are expressed here by \mathbf{q}^L and \mathbf{q}^R , respectively, for the sake of simplicity, $\mathbf{F}_k(\mathbf{q}) \cdot \mathbf{n}_k$ can be obtained with this solver as

$$\mathbf{F}_k(\mathbf{q}) \cdot \mathbf{n}_k = \begin{cases} \mathbf{F}^L & \text{if } 0 \leq S^L, \\ \mathbf{F}_*^L & \text{if } S^L < 0 \leq S^M, \\ \mathbf{F}_*^R & \text{if } S^M < 0 \leq S^R, \\ \mathbf{F}^R & \text{if } S^R < 0, \end{cases} \quad (27)$$

where, S^L, S^M and S^R are the left, middle (contact) and right wave speeds, respectively (Fig. 6). They can be approximated from the two-rarefaction assumption [69]. On unstructured grids, the left and right wave speeds, which take the dry bed into account, are expressed as

$$S^L = \begin{cases} u^{\perp L} - 2\sqrt{gh^L} & \text{if } h^L = 0, \\ \min(u^{\perp L} - \sqrt{gh^L}, u_*^{\perp} - \sqrt{gh_*}) & \text{if } h^L > 0, \end{cases} \quad (28)$$

$$S^R = \begin{cases} u^{\perp R} + 2\sqrt{gh^R} & \text{if } h^R = 0, \\ \max(u^{\perp R} + \sqrt{gh^R}, u_*^{\perp} + \sqrt{gh_*}) & \text{if } h^R > 0. \end{cases} \quad (29)$$

In Eqs. (28) and (29), u^{\perp} denotes the velocity normal to the considered edge and $u^{\perp} = un_x + vn_y$. The middle variables h_* and u_*^{\perp} are calculated from

$$h_* = \frac{1}{g} \left[\frac{1}{2} \left(\sqrt{gh^L} + \sqrt{gh^R} \right) + \frac{1}{4} (u^{\perp L} - u^{\perp R}) \right]^2, \quad (30)$$

$$u_*^{\perp} = \frac{1}{2} (u^{\perp L} + u^{\perp R}) + \sqrt{gh^L} - \sqrt{gh^R}. \quad (31)$$

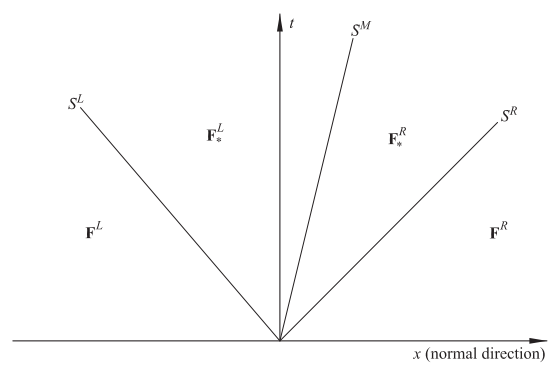


Fig. 6. HLLC solution of a local Riemann problem.

As proposed by Toro [70], the middle wave speed is evaluated by

$$S^M = \frac{S^L h^R (u^{\perp R} - S^R) - S^R h^L (u^{\perp L} - S^L)}{h^R (u^{\perp R} - S^R) - h^L (u^{\perp L} - S^L)}. \quad (32)$$

The interface fluxes $\mathbf{F}^L = \mathbf{F}(\mathbf{q}^L) \cdot \mathbf{n}_k$ and $\mathbf{F}^R = \mathbf{F}(\mathbf{q}^R) \cdot \mathbf{n}_k$ are computed by Eq. (7). As described in [15], \mathbf{F}_*^L and \mathbf{F}_*^R beside the contact wave are given by

$$\mathbf{F}_*^L = \begin{bmatrix} \mathbf{F}_{*1} \\ \mathbf{F}_{*2} n_x - u^{\parallel L} \mathbf{F}_{*1} n_y \\ \mathbf{F}_{*2} n_y + u^{\parallel L} \mathbf{F}_{*1} n_x \end{bmatrix}, \quad (33)$$

$$\mathbf{F}_*^R = \begin{bmatrix} \mathbf{F}_{*1} \\ \mathbf{F}_{*2} n_x - u^{\parallel R} \mathbf{F}_{*1} n_y \\ \mathbf{F}_{*2} n_y + u^{\parallel R} \mathbf{F}_{*1} n_x \end{bmatrix}, \quad (34)$$

where, u^{\parallel} is the velocity tangential to the considered edge and $u^{\parallel} = -u n_y + v n_x$. The middle flux $\mathbf{F}_* = [\mathbf{F}_{*1}, \mathbf{F}_{*2}]^T$ are computed with HLL formula [71] as

$$\mathbf{F}_* = \frac{S^R \mathbf{F}(\mathbf{q}^{\perp L}) - S^L \mathbf{F}(\mathbf{q}^{\perp R}) + S^L S^R (\mathbf{q}^{\perp R} - \mathbf{q}^{\perp L})}{S^R - S^L}. \quad (35)$$

In this equation, the normal variables $\mathbf{q}^{\perp} = [h, q_x n_x + q_y n_y]$ and $\mathbf{F}(\mathbf{q}^{\perp})$ is in the form of

$$\mathbf{F}(\mathbf{q}^{\perp}) = \begin{bmatrix} h u^{\perp} \\ u^{\perp} (q_x n_x + q_y n_y) + g h^2 / 2 \end{bmatrix}. \quad (36)$$

2.8. Slope source term treatment

Audusse and Bristeau [47] proposed a hydrostatic reconstruction method to preserve the C-property, for second order schemes on unstructured grids. With this method, the slope source terms in the considered cell (left cell in this work) can be transformed into fluxes through all edges of this cell, i.e.

$$\int_{\Omega} \mathbf{S}_b d\Omega = \oint_{\Gamma} \mathbf{F}_{Sk}(\mathbf{q}) d\Gamma, = \sum_{k=1}^3 [\mathbf{F}_{Sk}(\mathbf{q}) l_k], \quad (37)$$

where, \mathbf{F}_{Sk} denotes the flux vector of the slope source terms, at the k th edge and normal to this edge. $\mathbf{F}_{Sk}(\mathbf{q}^n)$ at the midpoint of the considered edge is given by

$$\mathbf{F}_{SM}(\mathbf{q}) = \begin{bmatrix} 0 \\ F_{SM} \mathbf{n}_M \end{bmatrix} = \begin{bmatrix} 0 \\ (\mathbf{F}_{SM}^I + \mathbf{F}_{SM}^C) \mathbf{n}_M \end{bmatrix}, \quad (38)$$

where, F_{SM} is the value of the slope flux \mathbf{F}_{Sk} , \mathbf{F}_{SM}^I and \mathbf{F}_{SM}^C denote the interface part and the centered part, respectively, and

$$\mathbf{F}_{SM}^I = \frac{g}{2} \left[(h_M^L)^2 - (\hat{h}_M^L)^2 \right], \quad (39)$$

$$\mathbf{F}_{SM}^C = -\frac{g}{2} (\hat{h}_M^L + h_i) (z_{bM}^L - z_{bi}), \quad (40)$$

in which, $\mathbf{n}_M = (n_{Mx}, n_{My})^T$; \hat{h}_M^L is the original water depth on the left hand side of the edge, and can be computed directly from Eq. (20); h_M^L and z_{bM} are the modified values obtained with Eqs. (25) and (24), respectively; h_i and z_{bi} denote the water depth and bed elevation of the considered cell, respectively. The values of \mathbf{F}_{SM}^I and \mathbf{F}_{SM}^C are illustrated by the areas of trapezoids in Fig. 7, for both dynamic and static flows. This slope source term treatment, in conjunction with the interface fluxes computed by the modified flow variables, can satisfy the C-property even at wet-dry interfaces [47].

For the static case shown in Fig. 7(b), since $h_i + z_{bi} = \hat{h}_M^L + z_{bM}^L = h_M^L + z_{bM}$, we obtain that

$$\begin{aligned} \mathbf{F}_{SM}^I + \mathbf{F}_{SM}^C &= \frac{g}{2} \left[-(h_M^L + h_i) (h_i - h_M^L) \right] \\ &= \frac{g}{2} \left[-(h_M^L + h_i) (z_{bM} - z_{bi}) \right]. \end{aligned} \quad (41)$$

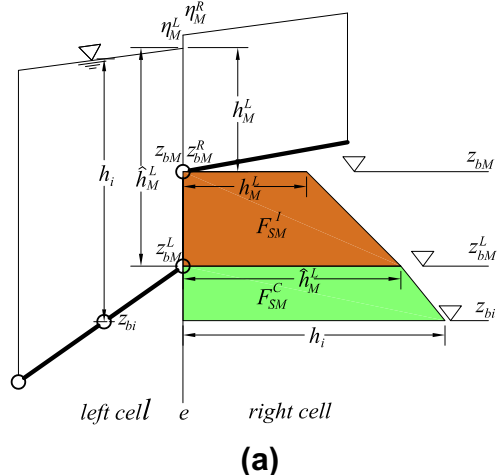
Obviously, this value is equivalent to the slope source term caused by the virtual bed, which is indicated by a dashed line connecting z_{bi} and z_{bM} , in Fig. 7(b). It means the forces on the water body under the virtual bed are balanced and do not affect the momentum change of this cell. This ideal is extended here to dynamic flows, by introducing a virtual bed and ignoring the influence of the water body under the virtual bed (Fig. 8(a)). As a result, the slope flux at the considered edge is rewritten as

$$F_{SM} = \frac{g}{2} \left[-(h_M^L + h_i) (z_{bM} - z_{bi}) \right]. \quad (42)$$

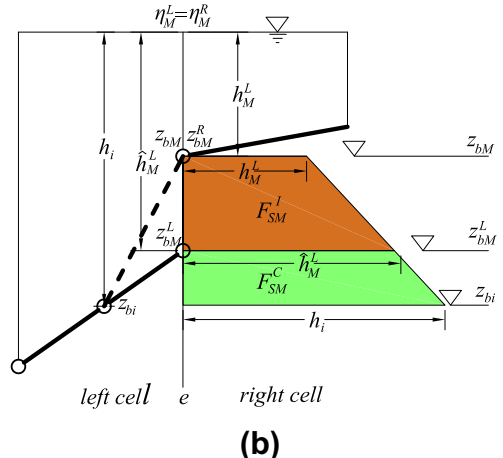
The value of F_{SM} is also shown in Fig. 8(a). Furthermore, in order to preserve the C-property for the cells with wet-dry interfaces (Fig. 8(b)), z_{bM} must be modified and thus the final slope flux is given by

$$z_{bM} \leftarrow \min(z_{bM}, \eta_M^L), \quad (43)$$

$$\mathbf{F}_{SM}(\mathbf{q}) = \begin{bmatrix} 0 \\ -n_{Mx} g (h_M^L + h_i) (z_{bM} - z_{bi}) / 2 \\ -n_{My} g (h_M^L + h_i) (z_{bM} - z_{bi}) / 2 \end{bmatrix}. \quad (44)$$



(a)



(b)

Fig. 7. Audusse's slope source term treatment at edge e of the left cell for: (a) dynamic flow, (b) static flow.

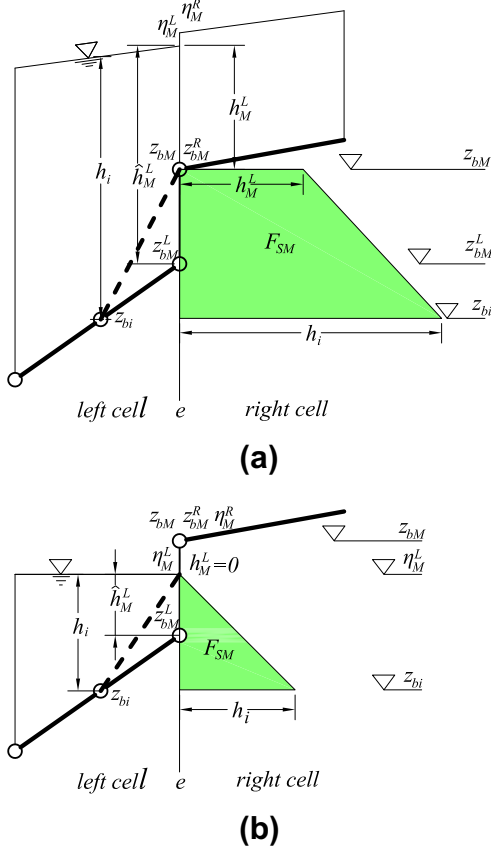


Fig. 8. Proposed slope source term treatment at edge e of the left cell: (a) for dynamic flow, (b) for static flow and e is wet-dry interface.

Although the resulting slope flux shown in Eq. (44) is in the same form as that in [35], the different derivation in this work can better understand the physical implication of Eq. (44) by means of a virtual bed. Furthermore, since a local modification of bed elevation is directly carried out in the slope source treatment in this work (Eqs (43) and (44)), the water depths used to compute the interface fluxes and slope source terms can be modified by the hydrostatic reconstruction from Eq. (25) instead of Eq. (16) in [35]. The former is slight simpler than the latter but the same results can be produced as proven in Appendix A.

In addition, compared to the Audusse's slope source term treatment, the new one is much simpler in form, and thus is a more economical method. It should be noted that, for dynamic flows, the forces on the water body under the virtual bed may not be strictly balanced. However, the influence is very little in general, e.g. F_{SM} in Fig. 8(a) is quite close to $\mathbf{F}_{SM}^I + \mathbf{F}_{SM}^C$ in Fig. 7(a). As demonstrated in corresponding test cases, the accuracy of the new treatment is nearly the same as that of the Audusse's one. It should also be stressed that for static case, due to the same values of slope flux and the same modified water depths which are used to compute the interface fluxes as those in [47], the proposed scheme in this work is also able to preserve the C-property.

2.9. Friction source term treatment

Like that in [5–7,35], the friction source terms are evaluated by a splitting point-implicit method [72], which is equivalent to solve the following ordinary differential equation

$$\frac{d\mathbf{q}}{dt} = \mathbf{S}_f. \quad (45)$$

In this section, $\mathbf{q} = (q_x, q_y)^T$. If Eq. (45) is discretized with implicit method, it becomes

$$\frac{\mathbf{q}^{n+1} - \mathbf{q}^n}{\Delta t} = \mathbf{S}_f^{n+1}. \quad (46)$$

Two components of \mathbf{S}_f^{n+1} can be rewritten into first order Taylor series as

$$\begin{aligned} \mathbf{S}_{fx}^{n+1} &= \mathbf{S}_{fx}^n + (\partial \mathbf{S}_{fx}/\partial \mathbf{q}_x)^n \Delta \mathbf{q}_x, \\ \mathbf{S}_{fy}^{n+1} &= \mathbf{S}_{fy}^n + (\partial \mathbf{S}_{fy}/\partial \mathbf{q}_y)^n \Delta \mathbf{q}_y, \end{aligned} \quad (47)$$

where, $\Delta \mathbf{q} = \mathbf{q}^{n+1} - \mathbf{q}^n$. Substitution of Eq. (47) into Eq. (46) along with the rearrangement lead to

$$\begin{aligned} \mathbf{q}_x^{n+1} &= \mathbf{q}_x^n + \Delta t (S_{fx}/D_x)^n = \mathbf{q}_x^n + \Delta t \bar{S}_{fx}, \\ \mathbf{q}_y^{n+1} &= \mathbf{q}_y^n + \Delta t (S_{fy}/D_y)^n = \mathbf{q}_y^n + \Delta t \bar{S}_{fy}, \end{aligned} \quad (48)$$

where, \bar{S}_f is the implicit friction source term vector; \mathbf{D} is the implicit coefficient vector and

$$\mathbf{D} = [D_x, D_y]^T = [1 - \Delta t (\partial S_{fx}/\partial q_x)^n, 1 - \Delta t (\partial S_{fy}/\partial q_y)^n]^T. \quad (49)$$

Letting $\hat{q} = \sqrt{q_x^2 + q_y^2}$,

$$\mathbf{D} = \left[\begin{array}{l} 1 + \frac{\Delta t C_f}{h^2} \left(\hat{q} + \frac{q_x^2}{\hat{q}} \right) \\ 1 + \frac{\Delta t C_f}{h^2} \left(\hat{q} + \frac{q_y^2}{\hat{q}} \right) \end{array} \right]^n. \quad (50)$$

With Eq. (48), the friction source is taken into account and \mathbf{q}^n used to calculate the fluxes and slope source terms is updated by this \mathbf{q}^{n+1} , at the beginning of each time step.

In order to prevent the flow direction from being inverted due to unphysical high friction in Eq. (48), the implicit friction source terms are limited by Liang and Marche [5] as

$$\bar{S}_{fx} \leftarrow \begin{cases} \max \left(-q_x^n/\Delta t, \bar{S}_{fx} \right) & \text{if } q_x^n \geq 0, \\ \min \left(-q_x^n/\Delta t, \bar{S}_{fx} \right) & \text{if } q_x^n < 0, \end{cases} \quad (51)$$

$$\bar{S}_{fy} \leftarrow \begin{cases} \max \left(-q_y^n/\Delta t, \bar{S}_{fy} \right) & \text{if } q_y^n \geq 0, \\ \min \left(-q_y^n/\Delta t, \bar{S}_{fy} \right) & \text{if } q_y^n < 0. \end{cases} \quad (52)$$

2.10. Boundary conditions

In the work reported herein, boundary conditions are implemented by means of flux computation at boundaries. For an open boundary (transmissive boundary), the fluxes are calculated by the Riemann solver (Eq. (27)), whereas, for a solid boundary (reflective or wall boundary), the fluxes are calculated directly with Eq. (7). The theory of characteristics provides sufficient information to establish a relation to find out the unknown variables at boundaries [3,73,15]. Assuming that the right side of the boundary is outside the computational domain, the relation at the midpoint M of a boundary edge is given as

$$u_M^{LR} + 2\sqrt{gh_M^R} = u_M^{LL} + 2\sqrt{gh_M^L}, \quad (53)$$

where the superscript L and R represent the variables on the left and right sides of the boundary edge, respectively (Fig. 3).

2.10.1. Open boundary conditions

When using the Riemann solver to compute the fluxes at open boundaries, the values of flow variables on both sides of this boundary are required. The values on the inner side can be obtained with Eq. (20) incorporated with the adaptive method,

whereas, for those on the outer side, the local flow regime has to be considered:

2.10.2. Subcritical flow:

In this case, an inflow or outflow boundary condition can be imposed in the form of flow depth, velocity, or unit width discharge. If h_M^R is given, $u_M^{\perp R}$ can be computed with Eq. (53) as

$$u_M^{\perp R} = u_M^{\perp L} + 2\sqrt{gh_M^L} - 2\sqrt{gh_M^R}. \quad (54)$$

In the case of a velocity boundary condition, h_M^R can be evaluated with the same equation as

$$h_M^R = \frac{\left(u_M^{\perp L} + 2\sqrt{gh_M^L} - u_M^{\perp R} \right)^2}{4g}, \quad (55)$$

If the unit width discharge $q_M^{\perp R}$ is given at the boundary and

$$q_M^{\perp R} = h_M^R u_M^{\perp R}, \quad (56)$$

h_M^R and $u_M^{\perp R}$ can be computed from Eqs. (53) and (56). As a non-linear equation is formed for h_M^R , the Newton–Raphson iterative method is used in this work to solve it.

After h_M^R and $u_M^{\perp R}$ are computed, u_M^R and v_M^R can be calculated by assuming that the tangential velocities at both sides of the boundary are the same [15]. It gives

$$\begin{aligned} u_M^R &= u_M^{\perp R} n_x - u_M^{\parallel R} n_y, \\ v_M^R &= u_M^{\parallel R} n_x + u_M^{\perp R} n_y. \end{aligned} \quad (57)$$

We then obtain $q_{xM}^R = h_M^R u_M^R$ and $q_{yM}^R = h_M^R v_M^R$.

2.10.3. Supercritical flow:

In the case of supercritical flow, h_M^R , q_{xM}^R and q_{yM}^R are prescribed at the inflow boundary and are equal to h_M^L , q_{xM}^L and q_{yM}^L , respectively, at the outflow boundary.

Finally, based on \mathbf{q}_M^R and \mathbf{q}_M^L , the fluxes at the boundary can be computed with Eq. (27), for both subcritical and supercritical flows.

2.10.4. Solid boundary conditions

At a solid boundary, the normal velocity is zero and the normal flux is simply computed with Eq. (7) as

$$\mathbf{F}(\mathbf{q}) \cdot \mathbf{n} = \begin{bmatrix} 0 \\ g(h_M^R)^2 n_x/2 \\ g(h_M^R)^2 n_y/2 \end{bmatrix}. \quad (58)$$

In this work, $h_M^R = h_M^L$ is adopted as that in [73,4,15].

Last but not least, the bed elevations on the left and right sides of a boundary are assumed as the same. As a result, z_{bM} can be evaluated with Eq. (24) as

$$z_{bM} = z_{bM}^L. \quad (59)$$

2.11. Stability criterion

A careful selection of the time step is required for an explicit scheme to maintain its stability. In this work, the Courant–Friedrichs–Lowy condition proposed in [18,19] is applied to estimate the time step on triangular grid. It can be expressed as

$$\Delta t = \text{CFL} \min \left(\frac{R_i}{\sqrt{u_i^2 + v_i^2 + \sqrt{gh_i}}} \right), \quad (60)$$

where, R_i is the minimum distance from the centroid to the edges of the i th triangle, CFL is the Courant number specified in the range $0 < \text{CFL} \leq 1$ and $\text{CFL} = 0.5$ is adopted in this work.

2.12. Main procedure of the model's application in a cell

In the i th cell, the procedure of the model to update the values of flow variables to the new time level can be summarized as the following steps:

- Step 1: The values of variables \mathbf{q}_i^n are updated with Eq. (48) to take the friction source terms into account.
- Step 2: In this cell, the adaptive method is applied to select a suitable scheme to extrapolate the values at the midpoint M of the considered edge (Eq. (23)). If the MUSCL reconstruction meets the condition, Eq. (20) will be used. Otherwise, the values are considered the same as those at the cell centroid.
- Step 3: The values at M are modified by the hydrostatic reconstruction with Eqs. (24)–(26).
- Step 4: The modified values are then employed in HLLC approximate Riemann solver to compute the interface fluxes of mass and momentum (Eq. (27)).
- Step 5: The modified values are also employed in Eq. (44) to compute the slope fluxes.
- Step 6: \mathbf{q}_i^{n*} are calculated with Eqs. (10) and (11) by summing the fluxes at all edges of this cell.
- Step 7: Finally, \mathbf{q}_i^{n+1} are obtained with Eqs. (9) and (11) by repeating Step 1 to Step 6, in which \mathbf{q}_i^{n*} are adopted as independent variables.

3. Test cases

In this section, several benchmark tests including analytical tests, experiments and a real dam-break case with measured data are applied to validate the present model.

In certain test cases, the norm L_K of error is used to reflect the deviation of the numerical solution from the analytical one quantitatively. For unstructured grids, volume weighted L_K error has to be used [74], formulated as

$$L_K(\mathbf{q}) = \left(\frac{\sum_i^{N_c} (A_i |\mathbf{q}_i - \tilde{\mathbf{q}}_i|^K)}{\sum_i^{N_c} A_i} \right)^{\frac{1}{K}}, \quad (61)$$

where, A_i is the volume of the i th cell; \mathbf{q}_i and $\tilde{\mathbf{q}}_i$ are the numerical and analytical solutions at the cell centroid, respectively; N_c denotes the number of cells.

For steady state solutions, convergence of the numerical solution is indicated by the global relative error, which is proposed by Zhou et al. [26] and is weighted by cell volumes for unstructured grids. It reads as

$$R(\mathbf{q}) = \sqrt{\frac{\sum_i^{N_c} \left[A_i \left(\frac{\mathbf{q}_i^n - \mathbf{q}_i^{n-1} \mathbf{n}}{\mathbf{q}_i^n} \right)^2 \right]}{\sum_i^{N_c} A_i}}. \quad (62)$$

The solution is taken as having converged to steady state if $R(h) < 1 \times 10^{-6}$.

3.1. Quiescent water around an island

The first test case is designed to verify the present model indeed preserves the C-property. In this test case, an island with the bed elevation of

$$z_b(x, y) = \max\{0, 2000 - 0.00032 \times [(x - 4000)^2 + (y - 4000)^2]\}, \quad (63)$$

is partially submerged in quiescent water with a constant surface level of 1000 m (Fig. 9). An 8000 m × 8000 m domain and a Delaunay triangular grid with 4256 cells are chosen. The model is run until $t = 10,000$ s with a constant time step $\Delta t = 2$ s. Quiescent water is observed throughout and the computed results at $t = 10,000$ s are plotted in Figs. 9 and 10. They indicate that the C-property is strictly preserved by this model, in the case involving uneven bed and wet-dry interfaces.

3.2. Transcritical flow over a bump

This test case is often used to verify the treatment of slope source terms of a model, and its ability to converge to a non-stationary steady state [26,46,10,75,52,4,50,35]. The flow occurs in a 25 m long and 1 m wide frictionless channel whose bed elevation is defined by

$$z_b(x) = \max[0, 0.2 - 0.05 \times (x - 10)^2]. \quad (64)$$

A transcritical flow is produced by imposing $h = 0.33$ m and $q_x = 0.18 \text{ m}^2/\text{s}$, on the right and left boundaries, respectively. Besides, $\eta^0 = 0.3$ m and $q_x^0 = 0.18 \text{ m}^2/\text{s}$ are initiated all over the domain. A regular Delaunay triangular grid with 3990 cells is chosen. The model is run until a steady state is achieved, using $\Delta t = 0.005$ s. The convergence processes reflected by a global relative error, are plotted in Fig. 11. The present model is able to reach a steady state defined by $R(h) < 1 \times 10^{-6}$, for both the new slope source term treatment and the Audusse's one, after about 28,000 iterations. A better performance than that of the LCD scheme proposed by Hubbard [38] is observed, because the limiter of the latter is not differentiable.

The steady results along the centerline of the channel are sketched in Fig. 12. A good agreement of the numerical results with the analytical solutions is observed, though minor oscillations of the numerical q_x occur near the turning point of water level. Those oscillations are normal problems for the implementation of a second order scheme in such a case and can also be found for example in [26,46,10,75,52,4,50,35]. The results of the Audusse's slope source term treatment are nearly the same with those of the new slope source term treatment. As the latter has a simpler form, it makes the model 2.97% faster than that with the former. Thus, the new slope source term treatment is recommended.

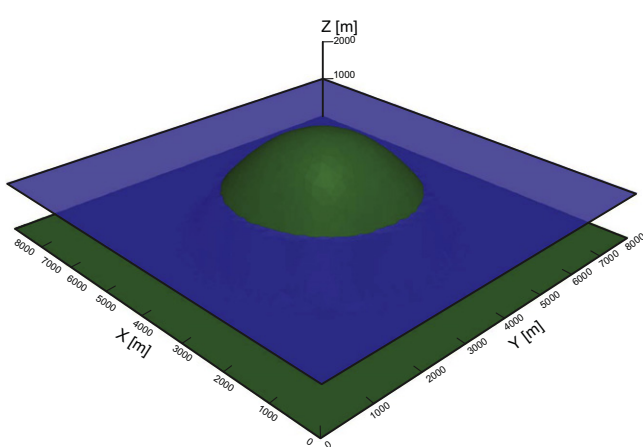


Fig. 9. Quiescent water around an island: 3D water level at $t = 10,000$ s and the island elevation.

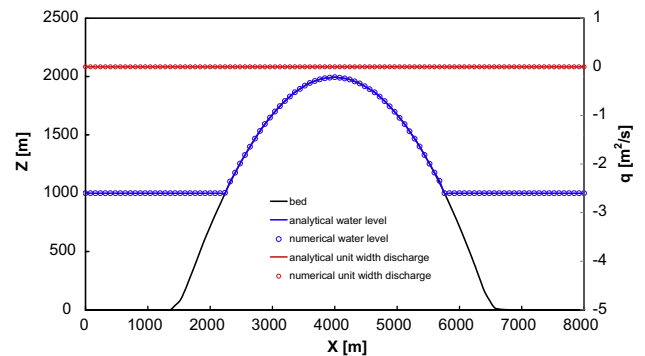


Fig. 10. Quiescent water around an island: analytical and computed water levels and discharges at the section $y = 4000$ m at $t = 10,000$ s.

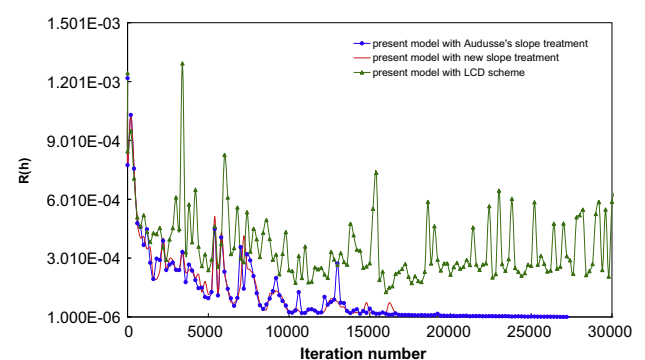


Fig. 11. Transcritical flow over a bump: temporal evolutions of relative errors.

3.3. Tidal wave over two steps

As shown in Fig. 13(a), a tidal wave flow occurs in a 1500 m × 100 m frictionless channel with two vertical steps. This case was proposed by the EU CADAM project [76] and was investigated later in [77,5]. It is used to validate the capability of the present model to deal with discontinuous bed, which is defined by

$$z_b(x) = \begin{cases} 8 & \text{if } |x - 750| \leqslant 187.5, \\ 0 & \text{otherwise.} \end{cases} \quad (65)$$

An asymptotic analytical solution of the flow is developed by Bermudez and Vazquez [37] as

$$h(x, t) = 20 - z_b(x) - 4 \sin \left[\pi \left(\frac{4t}{86400} + \frac{1}{2} \right) \right], \quad (66)$$

$$u(t) = \frac{(x - L)\pi}{5400h(x, t)} \cos \left[\pi \left(\frac{4t}{86400} + \frac{1}{2} \right) \right], v(t) = 0. \quad (67)$$

The initial conditions are specified by $h(x, 0)$ and $u(x, 0)$. $h(0, t)$ is imposed on the left boundary and the right one is solid wall. The simulation is run for 32,400 s with a Courant number of 0.5, on a Delaunay triangular grid with 7010 cells.

The computed water levels and velocities, along the centerline of the channel, are compared with the analytical solutions in Fig. 13(a)–(c). A satisfactory agreement confirms that the present model is able to handle the discontinuous topography. It should be noted, with the new slope source term treatment, the vertical steps are directly approximated by a very steep slope, which is equal to the ratio between the step height and about half of the grid size. This process is similar to that in [5]. Besides, the results computed with the new slope source term treatment and those computed with the Audusse's one [47] are quite close. In spite of

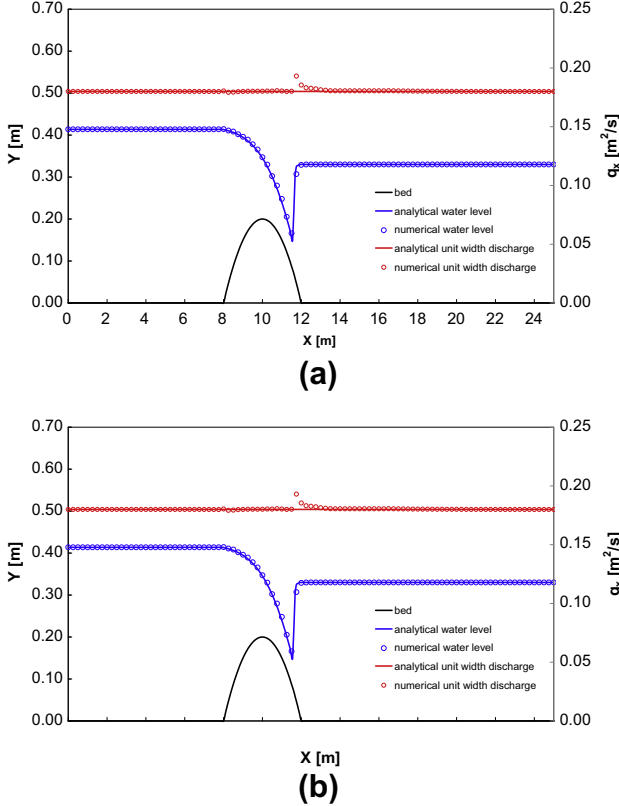


Fig. 12. Transcritical flow over a bump: profiles of water levels and discharges at centerline: (a) present model with new slope source treatment, (b) present model with Audusse's slope source term treatment [47].

this, the present model with the former is again verified to be 3.21% faster than that with the latter, and thus the former is recommended.

3.4. Laboratory dam-break wave over a triangular bottom sill

The present model is applied here to reproduce a laboratory dam-break wave over a triangular bottom sill. This experiment is a part of the IMPACT project [78] and the data are provided by Frazpo [79]. The setup and the initial conditions are illustrated in Fig. 14. The horizontal channel is 5.6 m long and 0.5 m wide. In this channel, a dam is located at $x = 2.39$ m and a reservoir is formed upstream with 0.111 m deep water. A symmetrical bump is installed at $x = 4.45$ m with a height of 0.065 m and bed slopes of ± 0.14 . A wall blocks the downstream end of the channel. Between the wall and the bump, a pool is filled initially with a water level of 0.02 m above the flat bed. The gate of the reservoir is removed suddenly when the experiment is started. Then, the water levels are measured around the bump and at three gauges, which are located in the centerline of the bed with $x = 5.575$ m, $x = 4.925$ m and $x = 3.935$ m, respectively (Fig. 14).

For the numerical simulation, a $5.6 \text{ m} \times 0.5 \text{ m}$ computational domain with four closed boundaries is used, and is discretized into 7720 triangular cells. The initial conditions are exactly set to be the same as those in the experiment. A Manning coefficient of $0.011 \text{ m}^{-1/3} \text{ s}$ is chosen following [79]. A Courant number of 0.5 is adopted and the simulation stops when $t = 45$ s. The computed water levels at three gauges and in the centerline around the bump are plotted in Figs. 15 and 16, respectively. The results of the present model with the new slope source term treatment agree closely with the measurements. It is verified again that, on unstructured

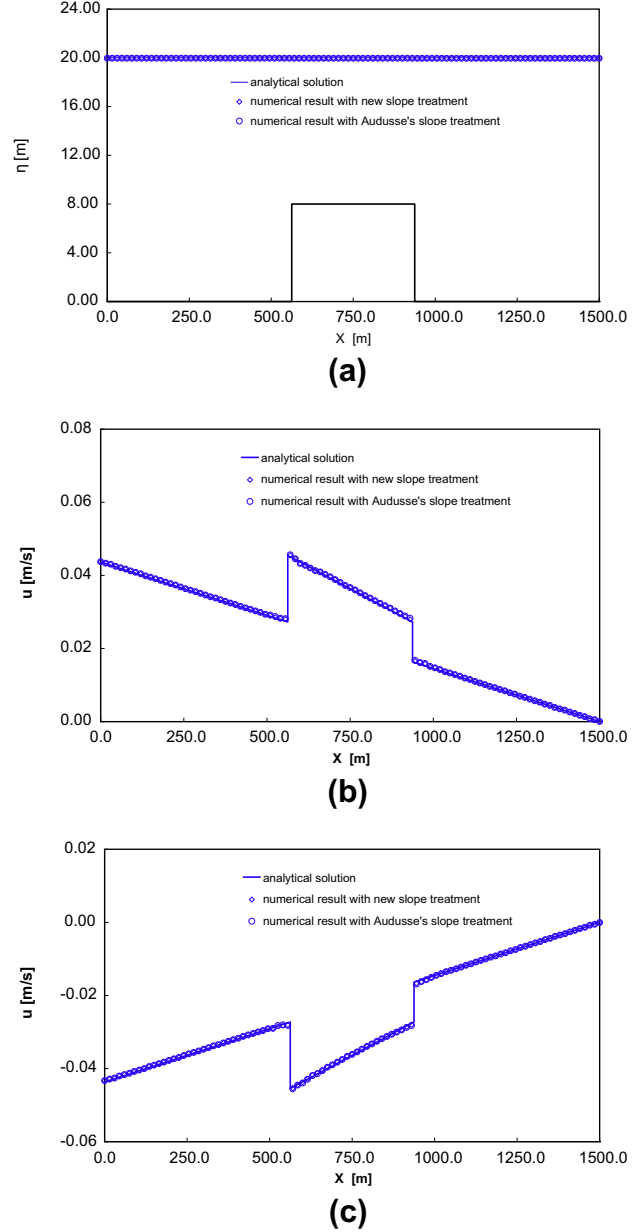


Fig. 13. Tidal wave over two steps: (a) water level profile at $t = 10,800$ s, (b) velocity profile at $t = 10,800$ s, (c) velocity profile at $t = 32,400$ s.

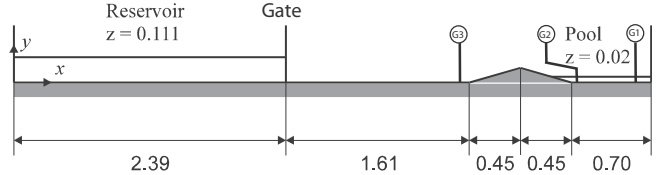
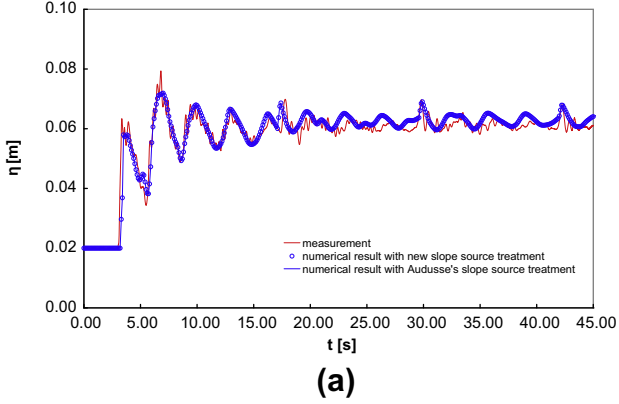
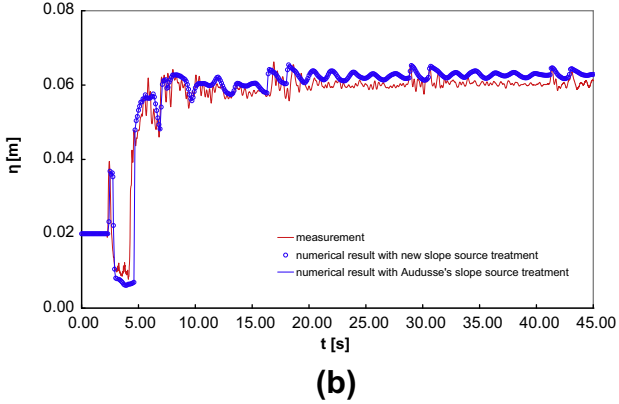


Fig. 14. Dam-break over a triangular bottom sill: experimental setup and initial conditions, all dimensions in meter [79].

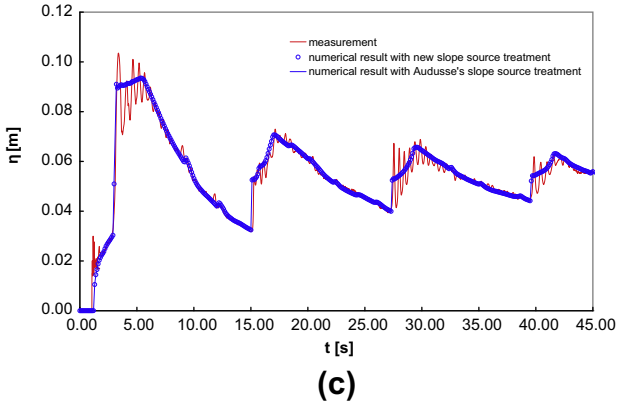
grid, the present model can produce satisfactory numerical results, for the case with uneven bed and wet-dry fronts. In addition, these results are consistent with those of the Audusse's one, but the model with the latter takes 3.13% more computational time. Therefore, the new slope source term treatment is better in terms of efficiency.



(a)



(b)



(c)

Fig. 15. Dam-break over a triangular bottom sill: time histories of water levels at: (a) gauge 1, (b) gauge 2, (c) gauge 3.

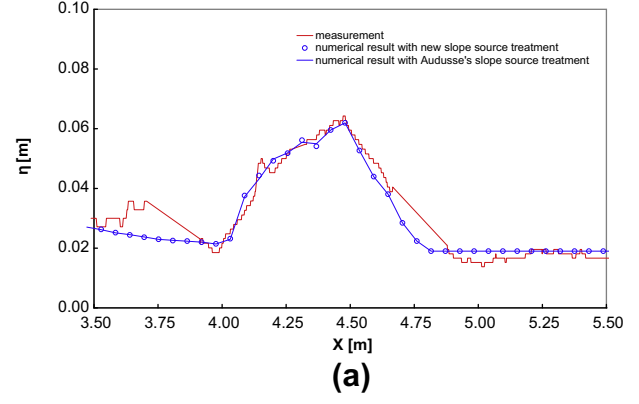
3.5. Thacker's planar solution

This test case is one of the most difficult cases for the numerical model since it involves a wetting and drying procedure inside a parabola, which is defined as

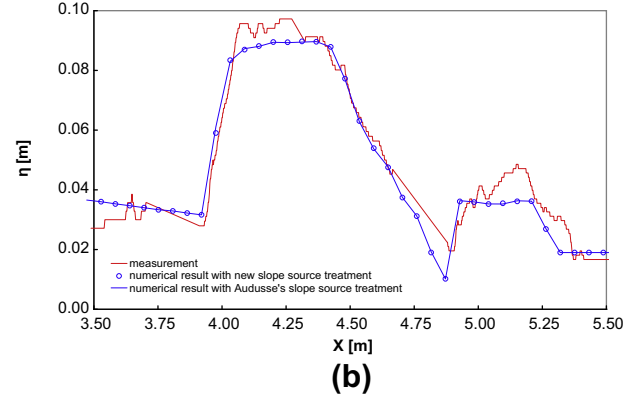
$$z_b(x, y) = -h_0 \left[1 - \frac{(x - x_0)^2 + (y - y_0)^2}{a^2} \right], \quad (68)$$

where, (x_0, y_0) is the center of the domain; h_0 is the depth of water at the center; a is the distance from the center to the zero elevation of the shoreline. As described in [68], if the bed friction is not taken into account, the analytical evolutions of water level and velocities can be calculated with the following equations

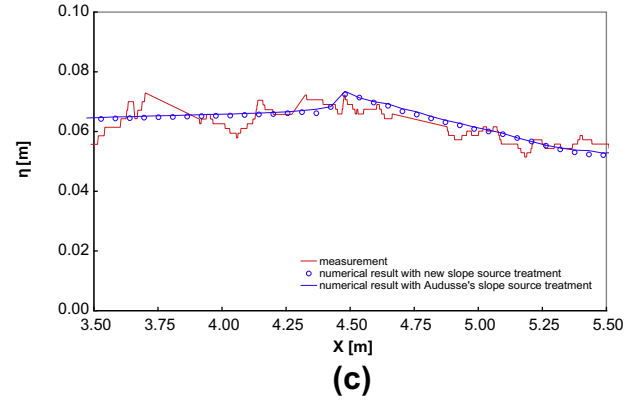
$$\eta(x, y, t) = \frac{\sigma h_0}{a^2} (2x \cos(\omega t) + 2y \sin(\omega t) - \sigma), \quad (69)$$



(a)



(b)



(c)

Fig. 16. Dam-break over a triangular bottom sill: water levels around the triangular sill at: (a) $t = 1.8$ s, (b) $t = 3.0$ s, (c) $t = 8.4$ s.

$$u(t) = -\omega \sigma \sin(\omega t), \quad v(t) = \omega \sigma \cos(\omega t), \quad (70)$$

in which, σ is a constant that determines the amplitude of the motion; $\omega = \sqrt{2gh_0}/a$ is the frequency of the rotation around the center of the domain. This solution has been used by a number of researchers in order to evaluate their numerical models, we refer for example in [60,17,80,15,19].

In this work, as shown in Fig. 17, a $4 \text{ m} \times 4 \text{ m}$ computational domain is chosen with four solid boundaries. A regular Delaunay triangular grid with 16,000 cells and a distorted one with 19,835 cells are applied (Fig. 17). They are termed as grid I and II, respectively. The parameters are set to be the same values as those in [60], i.e. $h_0 = 0.1 \text{ m}$, $a = 1.0 \text{ m}$ and $\sigma = 0.5 \text{ m}$. Evidently, the initial conditions are given by Eqs. (69) and (70) at $t = 0$ s. The water sloshing for four periods ($4T$) is simulated with a Courant number of 0.5.

The computed water levels and discharges at $t = 3.5T$ at cross-section A (Fig. 17) of grids I and II are plotted in Figs. 19 and 20,

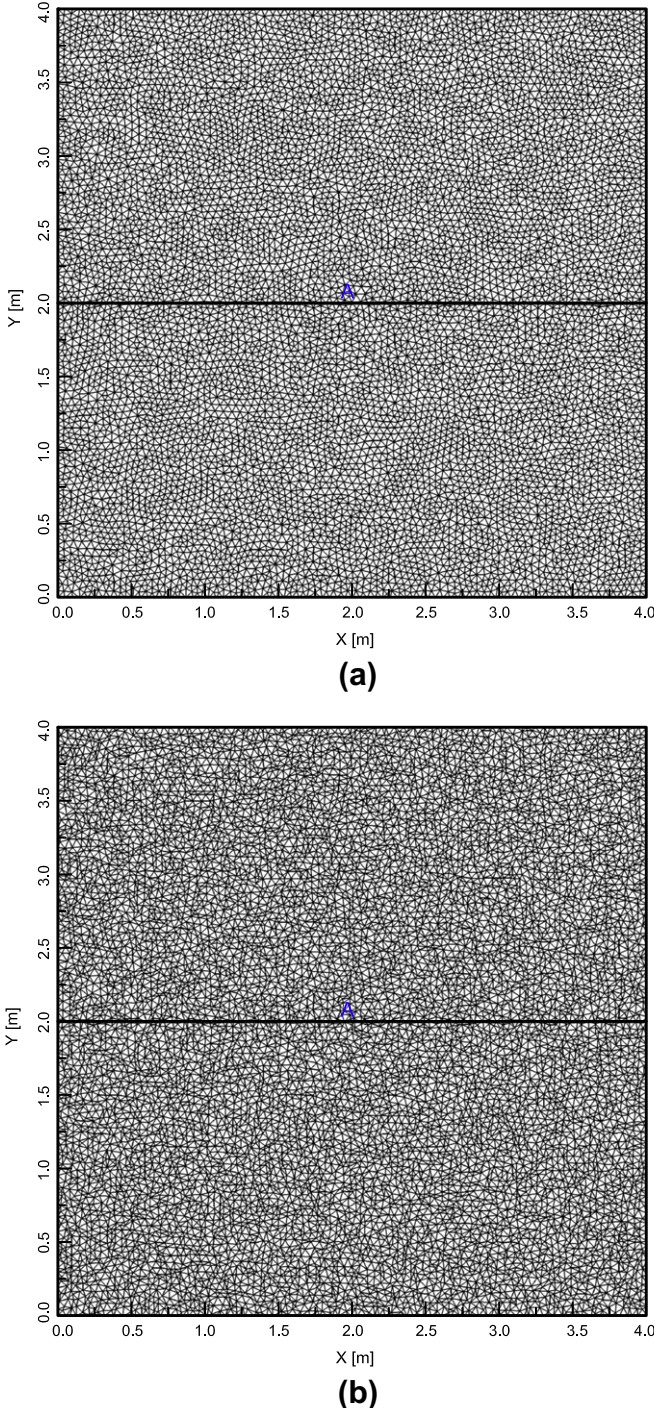


Fig. 17. Thacker's planar solution: computational domain and grids: (a) regular Delaunay grid (grid I), (b) distorted grid (grid II).

respectively. The results of the present model agree well with the analytical solutions on both grids. No obvious distortion is detected near wet-dry fronts. Figs. 19 and 20 also show the computed results of the new slope source treatment and those of the Audusse's one are very similar. However, since the former renders the present model 3.05% faster than that with the latter, the new slope source treatment is better. The similar accuracies of the two slope source treatments can also be reflected by very close L_1 errors in Fig. 21. In the same Figure, a much higher accuracy of the proposed MUSCL scheme than that of the first order scheme and the LCD scheme is demonstrated, for both grids. Moreover, as sketched in Fig. 18, unphysical high velocities and negative water depths

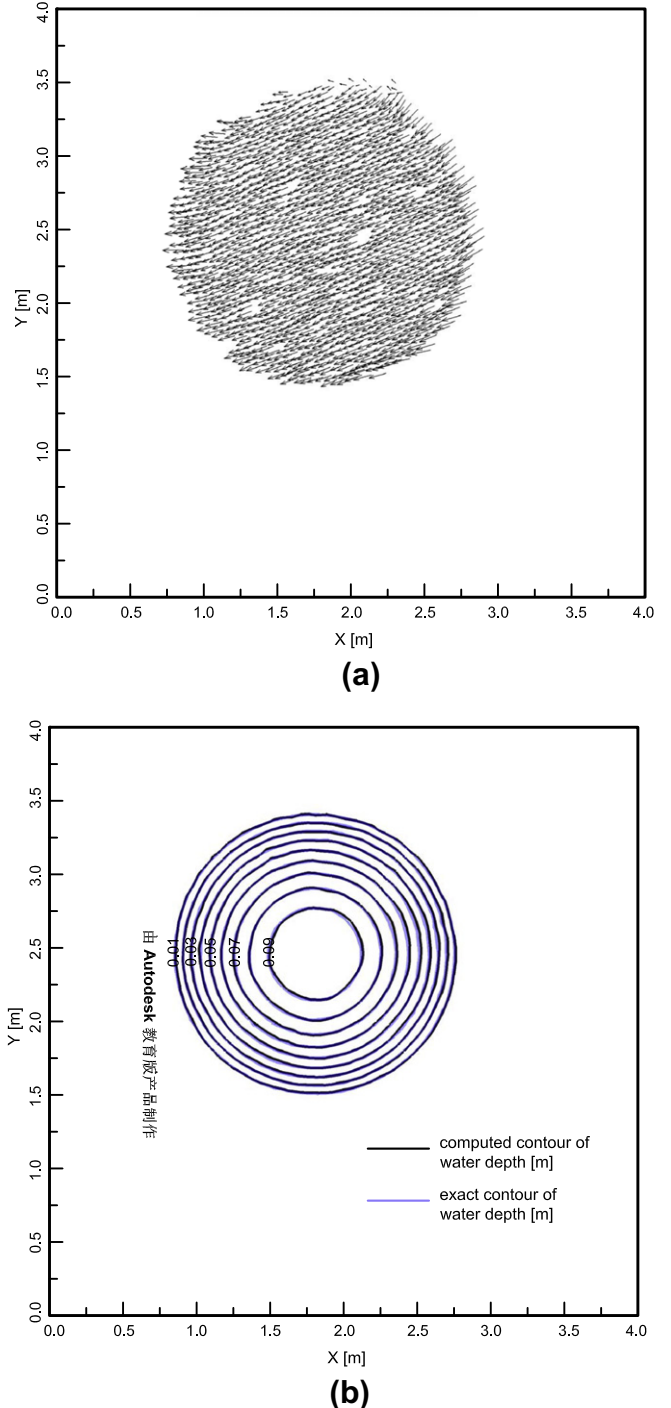


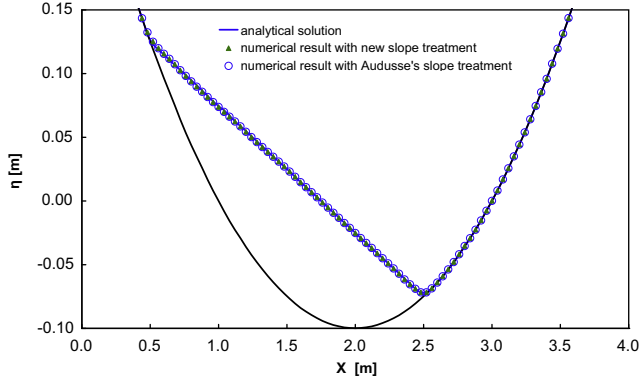
Fig. 18. Thacker's planar solution: computed flow field by the present model on grid I at $t = 5.9$ s: (a) velocities, (b) water depths.

shown in Fig. 4 are successfully prevented by the present model with the adaptive method.

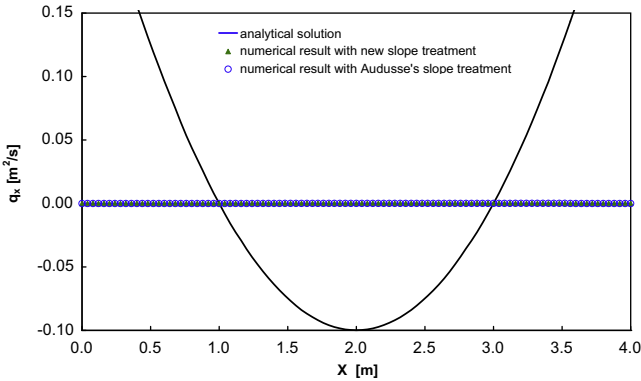
The mass conservation can be verified by the following formula [81,15]

$$\varepsilon_m = \max_t \left(\frac{|V^t - V^0 + \delta V^t|}{V^0} \right), \quad (71)$$

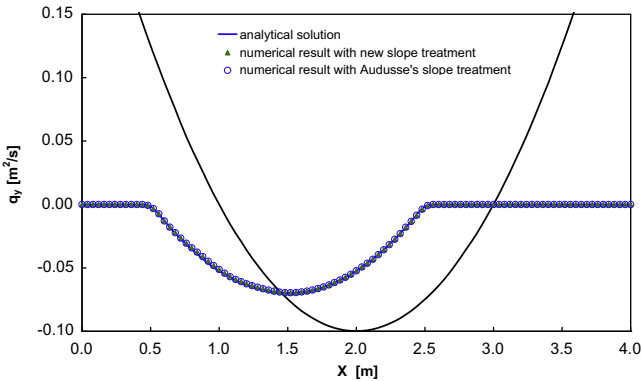
where ε denotes the maximum relative error in global mass conservation over the simulation duration; V^0 and V^t are the initial volume of water and the computed one at the time t , respectively; δV^t represents the net volume transported out of the domain from



(a)



(b)

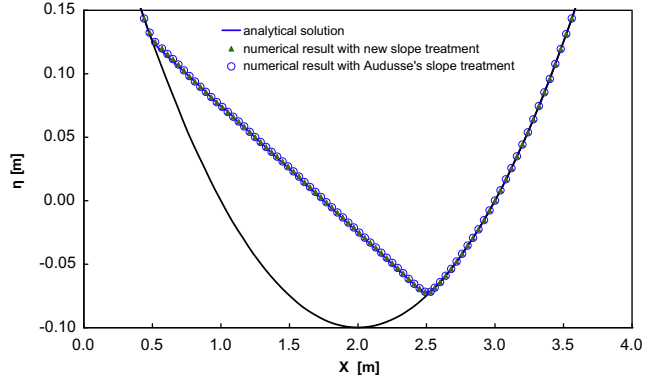


(c)

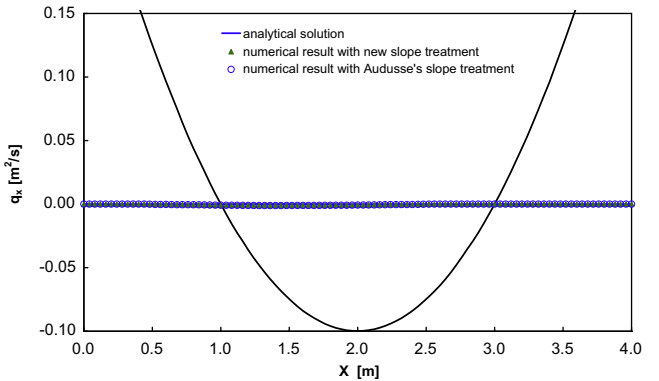
Fig. 19. Thacker's planar solution: numerical results on grid I at section A at $t = 3.5T$: (a) η , (b) q_x , (c) q_y .

the beginning to the time t , and $\delta V^t = 0.0$ in this case. ε_m is computed with Eq. (71) to be $6.3610233 \times 10^{-15}$ and 6.361059×10^{-15} on grids I and II, respectively, which are accurate up to round-off errors.

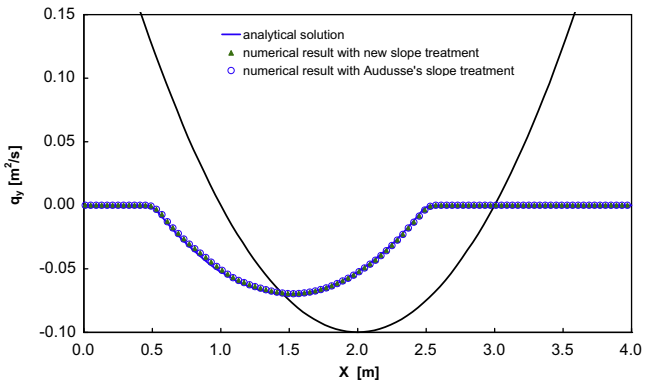
In this work, $\varepsilon_{wd} = 1 \times 10^{-6}$ m is used to identify wet and dry cells as that in [55,10,11,34], the sensitivity of the present model to ε_{wd} is investigated in this test case. Fig. 22 plots the L_1 errors of the water depth computed by the present model with different ε_{wd} on grid I. Evidently, the accuracy is very sensitive to the values of ε_{wd} higher than $\varepsilon_{wd} = 1 \times 10^{-6}$ m, whereas no obvious improvement of accuracy is observed when $\varepsilon_{wd} < 1 \times 10^{-6}$ m. Besides, the smaller ε_{wd} is, the more expensive the computation becomes, due to less so-called dry cells which only need first order scheme. For example, the present model with $\varepsilon_{wd} = 1 \times 10^{-6}$ m is 4.633% faster



(a)



(b)



(c)

Fig. 20. Thacker's planar solution: numerical results on grid II at section A at $t = 3.5T$: (a) η , (b) q_x , (c) q_y .

than that with $\varepsilon_{wd} = 1 \times 10^{-8}$ m. Therefore, $\varepsilon_{wd} = 1 \times 10^{-6}$ m is an appropriate wet-dry tolerance for the present model in this test case, in terms of accuracy and efficiency. Moreover, as demonstrated in other test cases, this value performs also well in capturing wet-dry fronts.

The grid convergence of the present model with the proposed MUSCL scheme is also investigated in this test case, on different types of grids (Fig. 23). The first order upwind scheme and the LCD scheme are also incorporated in the present model for the comparisons. Figs. 24 and 25 show the convergence results in terms of L_1 and L_2 errors, on regular Delaunay grids (type A) after a period. In these figures, Δx is the average of the cell length and is computed by $\Delta x = \sqrt{S}$, in which, S denotes the average of cell area. Obviously, the convergence rates (orders of accuracy) of the

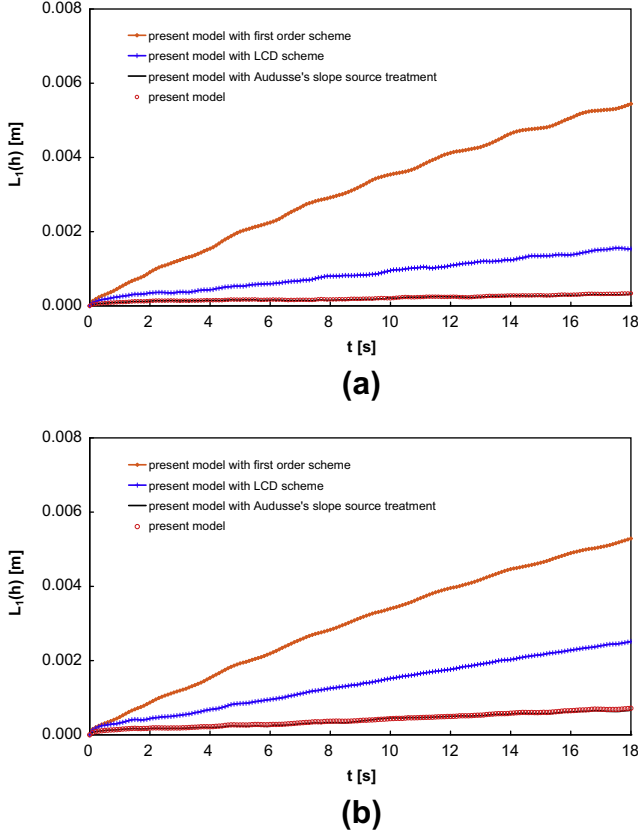


Fig. 21. Thacker's planar solution: L_1 errors of water depth on (a) grid I, (b) grid II.

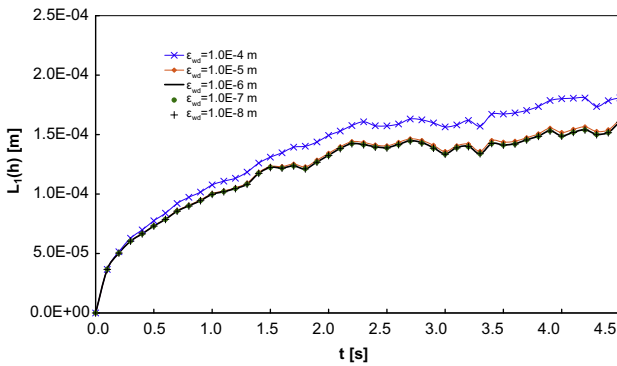


Fig. 22. Thacker's planar solution: sensitivity of the present model to ϵ_{wd} on grid I.

proposed MUSCL scheme are higher than those of the first order scheme and the LCD scheme, for all flow variables. In Figs. 26 and 27, the convergence rates of the present model with the proposed MUSCL scheme, in both L_1 and L_2 errors, on four types of triangular grids are shown, respectively. For all flow variables, we see that the present model on the type-D grids is least accurate, since the midpoint M is outside the gradient volume, when using the three adjacent cells to compute the gradient [19]. Therefore, other types of grids are preferred for the present model in practical application. The convergence rates on the type-B and type-C grids are between those on the type-A and type-D grids. The highest order of convergence is achieved on the type-A grids. It is close to but a little lower than second order. This drop of accuracy is, in general, an expected behavior when dry fronts are included in the solution, and a similar behavior was presented in [82,58,39,18,19]. Never-

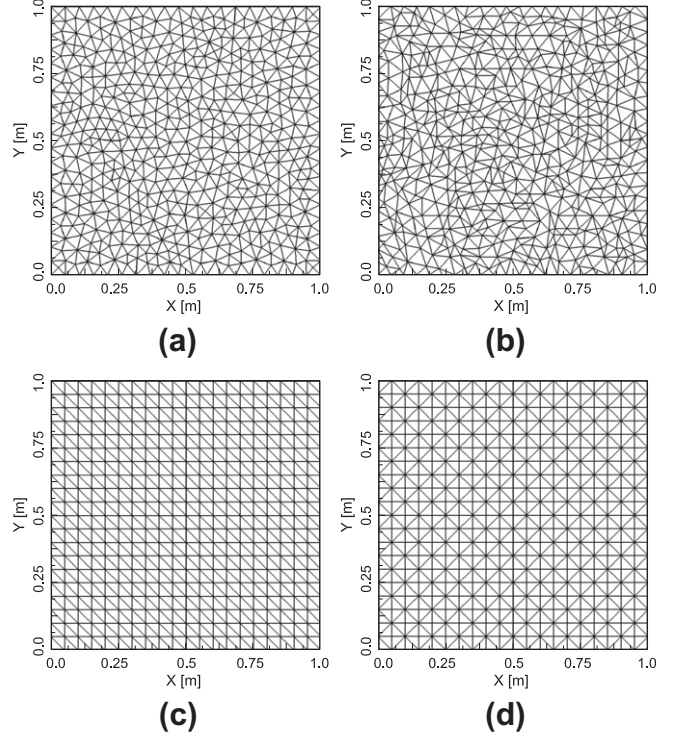


Fig. 23. Thacker's planar solution: different types of grids used to analyze grid convergence: (a) regular Delaunay grid (type A), (b) distorted triangular grid (type B), (c) orthogonal grid (type C), (d) orthogonal grid (type D).

theless, the numerical order of convergence is very satisfactory for this type of problem.

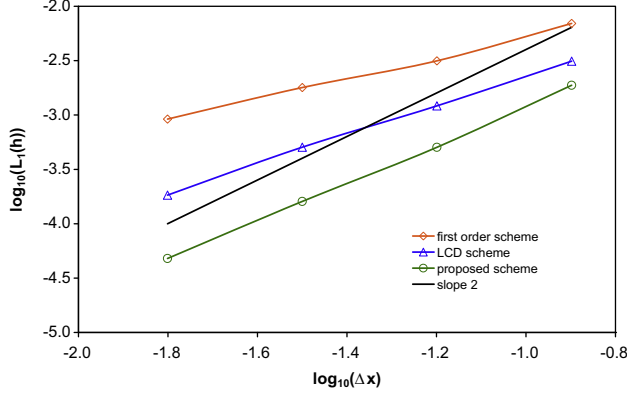
3.6. Dam-break flow in a channel with 45° bend

This test case is the first EU CADAM benchmark test [76], and was considered in [27,22,83] to test their model's capabilities to simulate dam-break. As sketched in Fig. 28, the experiment consists of a $2.39 \text{ m} \times 2.44 \text{ m}$ reservoir, and a 45° bending channel with a width of 0.495 m and a free outlet in the end. The bed of the reservoir is 0.33 m below that of the channel, forming a vertical step at the channel entrance. The water depth in the reservoir and channel is initiated as 0.58 m and 0 m , respectively. As for the Manning coefficient, a value of $0.0095 \text{ m}^{-1/3} \text{ s}$ is estimated as that in [27,22].

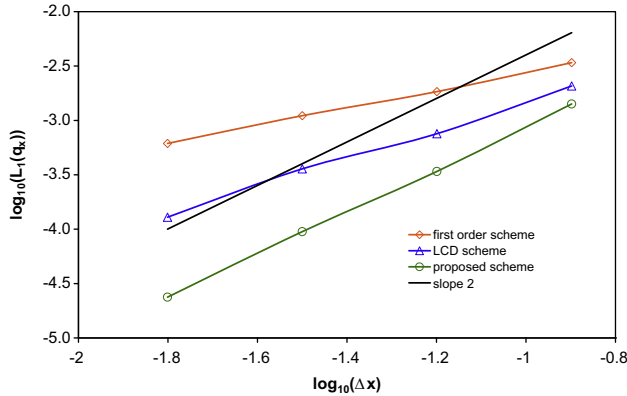
The simulation is run with a Courant number of 0.5, on a Delaunay triangular grid with 8976 cells (Fig. 28). The computed evolution of the dam-break wave at $t = 10 \text{ s}$ and 20 s are plotted in Fig. 29. Moreover, the time histories of the computed water levels, at the considered gauges G4, G6 and G9 (see Fig. 28), are compared with the measurements in Fig. 30. Both the arrival times and water levels are well predicted by the present model with the new slope source term treatment. These results are slightly better than those for example in [27,22], and are comparable with those for example in [83]. They indicate that the present model is sufficient for a dam-break flow simulation, over dry bed even with discontinuity, and on unstructured grids with irregular geometric boundaries.

3.7. Run-up of a solitary wave on a conical island

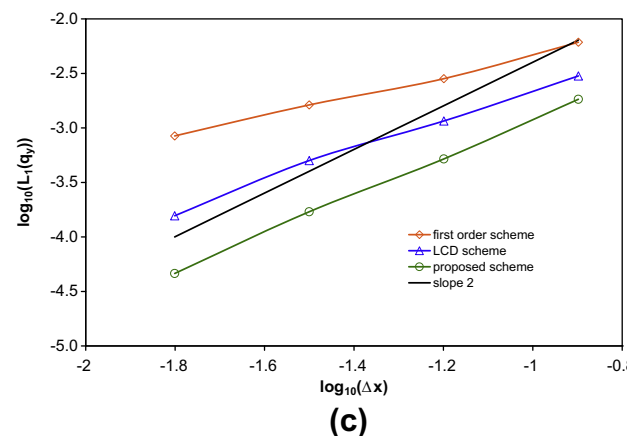
Briggs et al. [84] performed a series of experiments to study the run-up of tsunami waves on a conical island in the US Army Engineer Waterways Experiment Station. A conical island, which has a base diameter of 7.2 m , top diameter of 2.2 m and a height of 0.625 m , is located near the center of a $30 \text{ m} \times 25 \text{ m}$ basin. Solitary



(a)



(b)

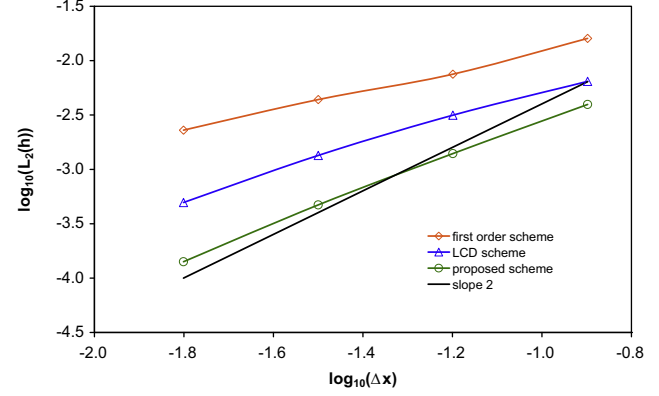


(c)

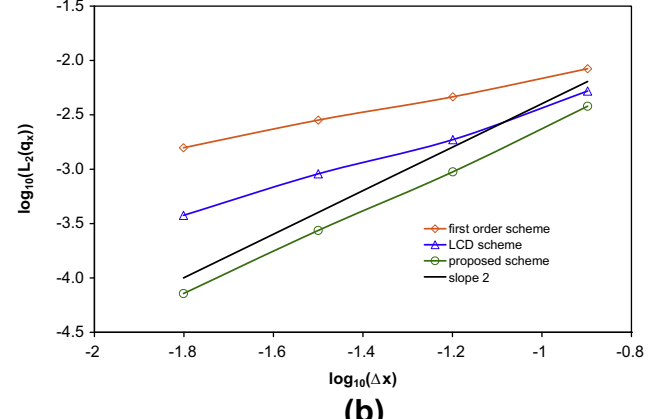
Fig. 24. Thacker's planar solution: convergence results of different schemes in L_1 errors at $t = T$ on regular Delaunay grids (type A) for: (a) η , (b) q_x , (c) q_y .

planar waves are generated by a directional wave-maker. The free surface water levels at a group of gauges and the maximum run-up on the island are measured. As the moving wet-dry fronts on uneven bed are produced in this experiment, when the wave runs up on the island, it can be applied to test model's capability to cope with wetting and drying over complex bed, for example in [85,86,8,87–89,39].

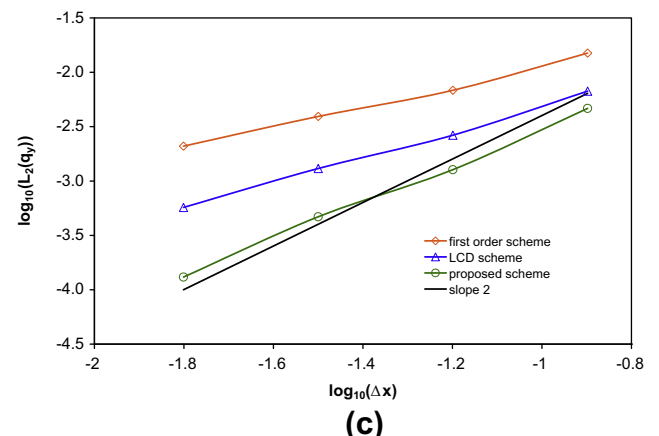
A $25.92 \text{ m} \times 27.6 \text{ m}$ computational domain is chosen here according to the length of the wave-maker (Fig. 31), thus the island is exactly located in the center. This simplification is reasonable, because the reflected wave by the wall opposite to the wave maker is not investigated in this work. Still water with a depth of 0.32 m is initiated in the domain. The left boundary is set to be the wave



(a)



(b)



(c)

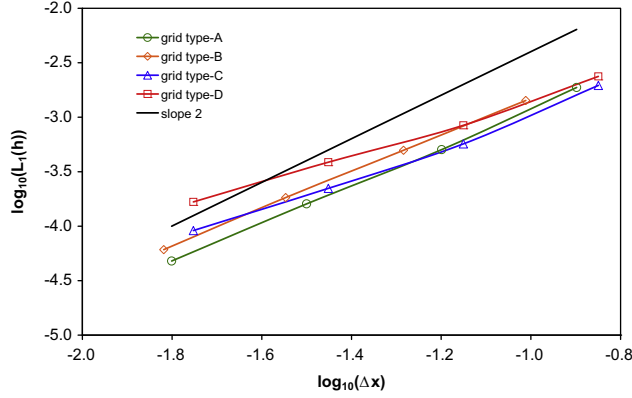
Fig. 25. Thacker's planar solution: convergence results of different schemes in L_2 errors at $t = T$ on regular Delaunay grids (type A) for: (a) η , (b) q_x , (c) q_y .

inflow boundary, where varying water level η (water level relative to the still water surface in this test case) and velocity u are imposed. As mentioned in [39], the wave inflow conditions obtained from the solitary wave theory are specified as

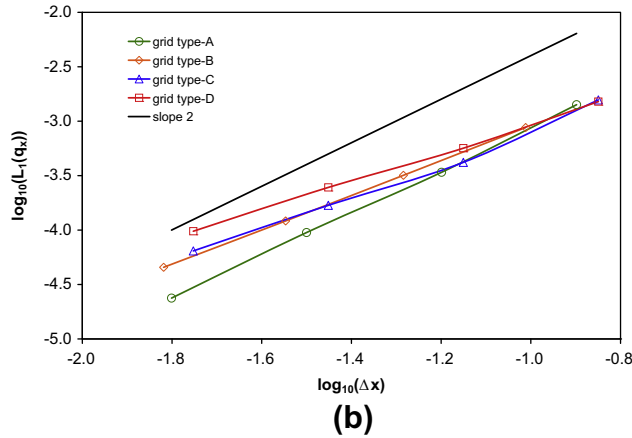
$$\eta(t) = H \operatorname{sech}^2 \left[\sqrt{\frac{3H}{4D}} C(t - T) \right], \quad (72)$$

$$u(t) = \frac{C\eta}{D + \eta}, \quad v(t) = 0, \quad (73)$$

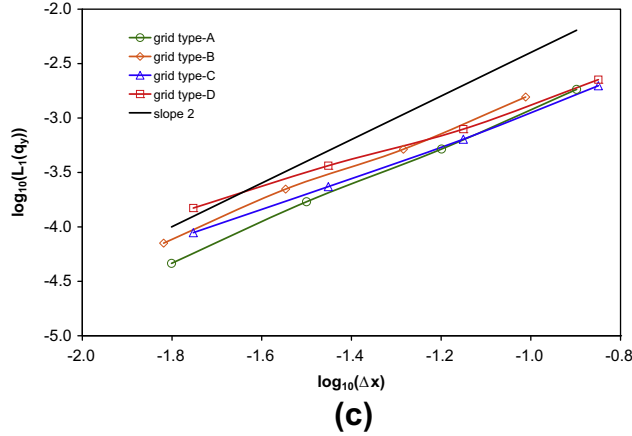
where, H is the amplitude of the incident wave and D is the still water depth; T denotes the time when the wave crests reach the



(a)



(b)

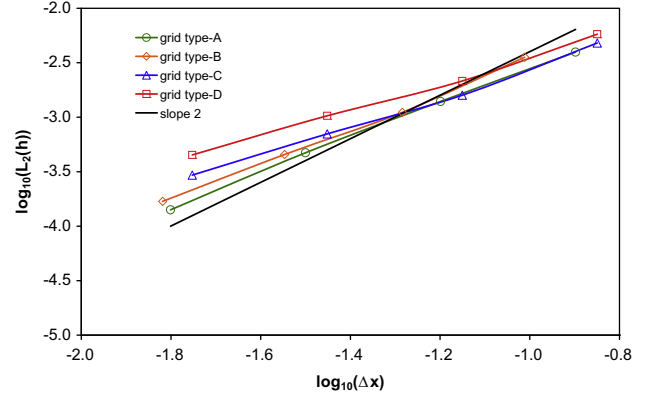


(c)

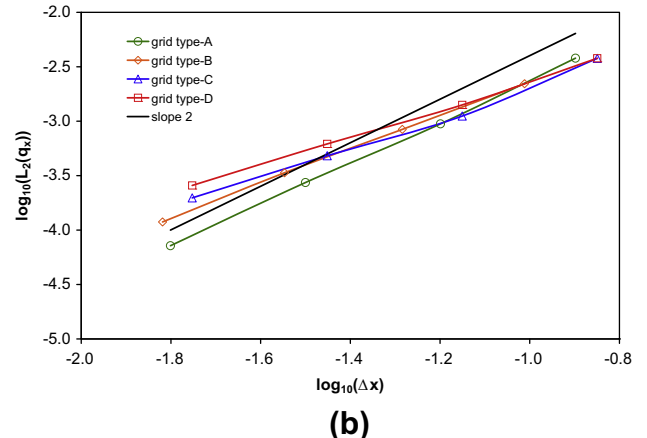
Fig. 26. Thacker's planar solution: convergence results of the present model in L_1 errors at $t = T$ on different types of grids for: (a) η , (b) q_x , (c) q_y .

domain and C is the wave celerity with $C = \sqrt{g(D + H)}$. In this work, a non-breaking incoming wave is chosen with $D = 0.32$ m, $H = 0.064$ m and $T = 2.45$ s (the first wave case in [39]). The rest of the boundaries are assumed to be closed as sketched in Fig. 31. Friction is not taken into account as that in [8,88,39]. A Courant number of 0.5 is chosen and the simulation is run until $t = 20.0$ s, on a Delaunay triangular grid with 82,998 cells.

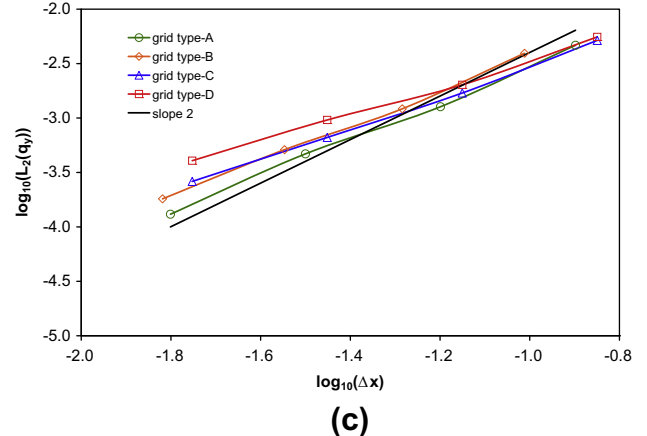
The simulated evolution of the solitary wave around the island is sketched in Fig. 34, where, the high run-up on the front side and the lee side of the island can be observed at $t = 9$ s and $t = 13$ s, respectively. The latter is generated by the collision of the two trapped waves on each side of the island as shown in Fig. 34(b). The simulated evolution is quite similar to that in [39].



(a)



(b)



(c)

Fig. 27. Thacker's planar solution: convergence results of the present model in L_2 errors at $t = T$ on different types of grids for: (a) η , (b) q_x , (c) q_y .

The simulated line of the maximum run-up on the island is compared with the measurements in Fig. 32, an overall close agreement is observed though with tiny discrepancies on the lee side. These discrepancies are in terms of a slightly over run-up and may be caused by the absence of friction. In addition, the computed and measured water levels at five wave gauges (Table 1 and Fig. 31) are plotted in Fig. 33. Obviously, the present model does a good job of predicting the lead wave heights and the arrival times at most gauges. However, compared to the measurements, the steepness of the wave fronts and the secondary depression wave following the lead wave are not exactly reproduced, due to the 3D property in reality [89]. Similar discrepancies are also predicted by other researchers using different numerical models, e.g.

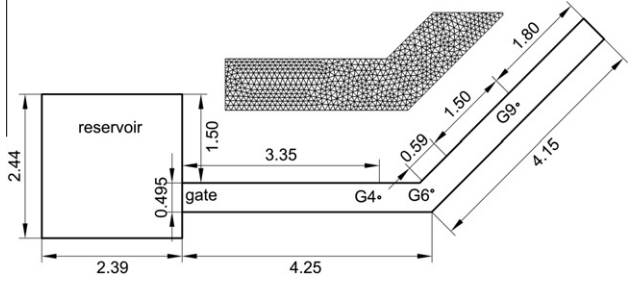


Fig. 28. Dam-break flow in a channel with 45° bend: plan view of the experimental setup, considered gauges and the mesh of the bend part.

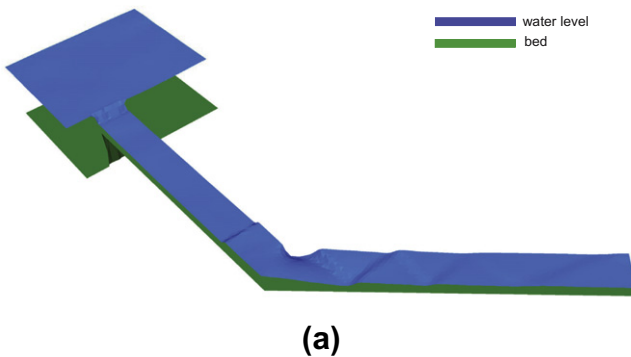


Fig. 29. Dam-break flow in a channel with 45° bend: evolution of the dam-break wave at: (a) $t = 10$ s, (b) $t = 20$ s.

in [90,87,88,39]. Furthermore, the predicted water levels at most gauges are quite close to those of [88,39], but the present model produces slightly better maximum wave heights, especially at WG 22. Therefore, the capability of the present model to handle wetting and drying over uneven bed are verified again by the satisfactory numerical results.

3.8. Flow involving wetting and drying over complex bed

This academic test case is designed here to test the performance of the present model in handling wetting and drying over strongly varying topography, on field scale. The computational domain is sketched in Fig. 35 and the topography is defined as

$$z_b(x, y) = \min[z_{b1}(x, y), z_{b2}(x, y), z_{b3}(x, y)], \quad (74)$$

where

$$z_{b1}(x, y) = \frac{(x + 250)^2}{1600} + \frac{y^2}{400}; \quad (75)$$

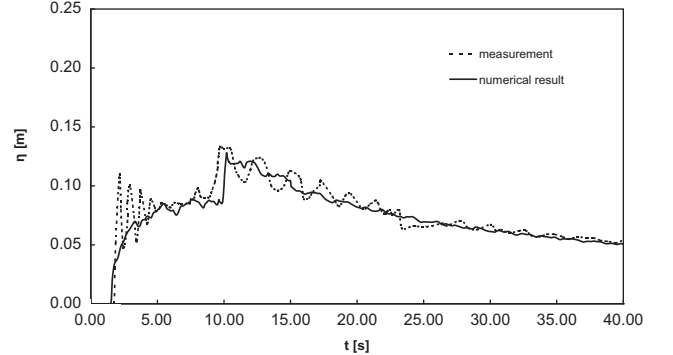


Fig. 30. Dam-break flow in a channel with 45° bend: time histories of water levels at: (a) G4, (b) G6, (c) G9.

$$z_{b2}(x, y) = \frac{x^2}{225} + \frac{(y - 50)^2}{225}; \quad (76)$$

$$z_{b1}(x, y) = \frac{(x - 250)^2}{1225} + \frac{y^2}{225} - 10. \quad (77)$$

Three bumps are integrated into the bed and are expressed by

$$z_{bb_1}(x, y) = \max \left[z_b(x, y), 80 - \frac{(x + 250)^2}{50} - \frac{y^2}{50} \right]; \quad (78)$$

$$z_{bb_2}(x, y) = 10 \text{ if } [(x - 200)^2 + (y + 10)^2] \leq 1000; \quad (79)$$

$$z_{bb_3}(x, y) = \max[z_b(x, y), 20] \text{ if } |x - 380| \leq 40 \text{ and } |y - 50| \leq 40. \quad (80)$$

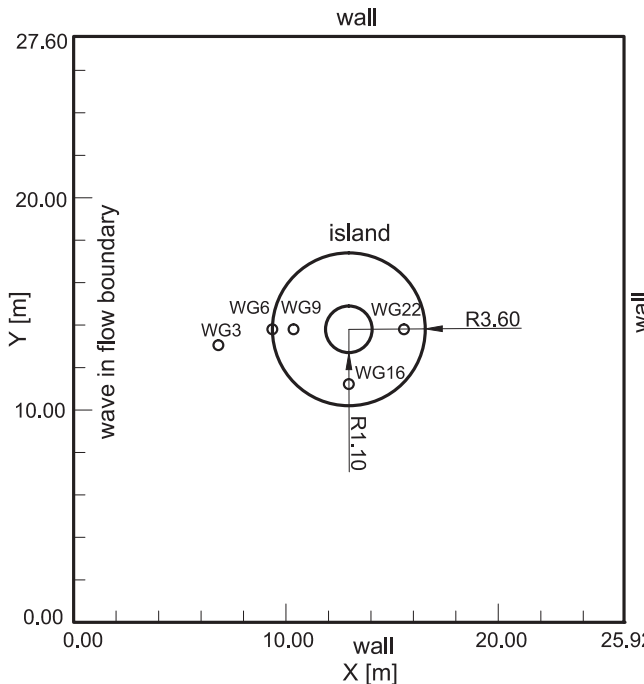


Fig. 31. Solitary wave run-up on a conical island: computational domain, boundary conditions and the locations of selected water-level gauges.

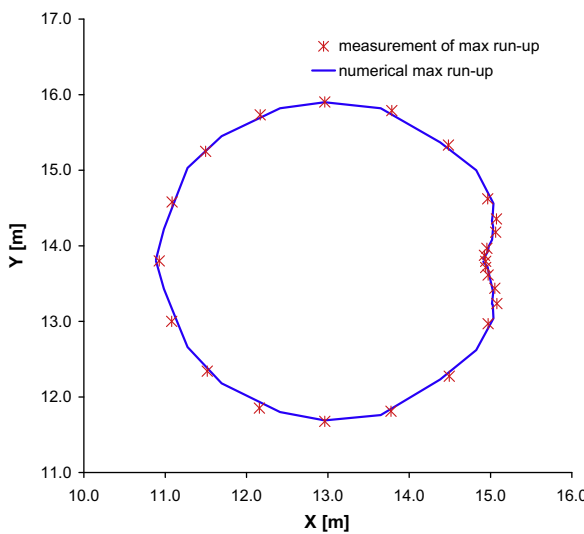


Fig. 32. Solitary wave run-up on a conical island: experimental and simulated maximum run-up.

Table 1
Locations of wave gauges.

Wave gauge	x	y
WG3	6.82	13.05
WG6	9.36	13.80
WG9	10.36	13.80
WG16	12.96	11.22
WG22	15.56	13.80

Finally, a strongly varying topography with discontinuities is formed as shown in Fig. 36(a).

The complex flow involving wetting and drying is produced by a dam-break. Initially, the water level in the reservoir ($x \leq -100$ m)

is assumed as $\eta^0 = 35$ m, and the rest of the domain is set to dry (Fig. 36(b)). All boundaries are closed and the Manning coefficient is considered equal to $0.033 \text{ m}^{-1/3}$ s. The simulation is carried out on an unstructured grid consisting of 29,206 triangular cells, with a Courant number of 0.5 (Fig. 36(a)). The computed evolution of the flood is plotted in Fig. 37 and we are interested in the wetting and drying processes. Fig. 37(a) presents the flood in a pit. Then the flood reaches the bump 2 and is separated (Fig. 37(b)). Fig. 37(c) shows the flood over the bump 2 and its front approaching the bump 3. Three lakes are gradually formed as shown in Fig. 37(d). During the simulation, no unphysical high velocities and negative water depths occur, e.g. the flow field in Fig. 35. These results indicate that the strong variations in the bottom topography do not affect the robustness of the present model.

3.9. Malpasset dam-break

The disastrous break of the Malpasset dam, which happened in the Reyran river valley in southern France in 1959, was frequently used as a benchmark test for a model to verify its capability to predict such risks [91,92,55,93,21,18,7,35]. In this work, the computational domain, the topographic data and the triangular grid provided in [91] are adopted (Figs. 38 and 39). The work of [91] also provides the field data including a police survey for high water marks at the survey points, and the flood arrival times at three electrical transformers (Fig. 38). In addition, the experimental water levels and the flood arrival times at certain gauges (Fig. 38), of a 1:400 scaled physical model, are available in [91].

The dam is simplified as a line segment with two ends whose coordinates are (4701.18 m, 4143.41 m) and (4655.50 m, 4392.10 m) (Fig. 38). Beside the dam, the floodplain is assumed initially dry, and the initial water level is considered equal to 100 m inside the reservoir. The only open boundary condition is the sea with a constant water level of 0 m. Friction is taken into account by setting Manning coefficient to $0.033 \text{ m}^{-1/3}$ s, which is proposed by the aforementioned researchers. The simulation is run with a Courant number of 0.5 until $t = 3600$ s.

The wave arrival times at the electrical transformers and the maximum water levels at survey points, computed with the present model, are compared with those of the field survey in Fig. 41(a) and (b). Good agreements are observed, although some discrepancies exist, especially for the maximum water levels. These discrepancies may be induced by the limitations of the 2D model in simulating 3D flows, by some uncertainties in survey and by the changes of the topography after the event. Besides, Fig. 40 illustrates the flood wave evolution at $t = 2000$ s, when the wave has already reached the downstream floodplain.

Fig. 42 compares the computed arrival times and the water levels, at the gauges of the physical model, with the experimental measurements. The present model exhibits an overall good agreement with the measured maximum water levels. But the computed wave propagates slightly slower than that of the physical model. A similar behavior can be found in [18,35]. In view of the fact that the arrival times at the transformers is more exactly simulated, scale effect, especially the roughness, may play an important role in distorting the wave propagation in the physical model [18]. As tested, a reduced Manning coefficient of $0.029 \text{ m}^{-1/3}$ s is able to produce better numerical results for the physical model, see Fig. 42.

4. Conclusions

A 2D well-balanced model is presented in detail to numerically solve SWEs on unstructured grids, within the framework of the Godunov-type cell-centered finite volume method. It owns the following new features:

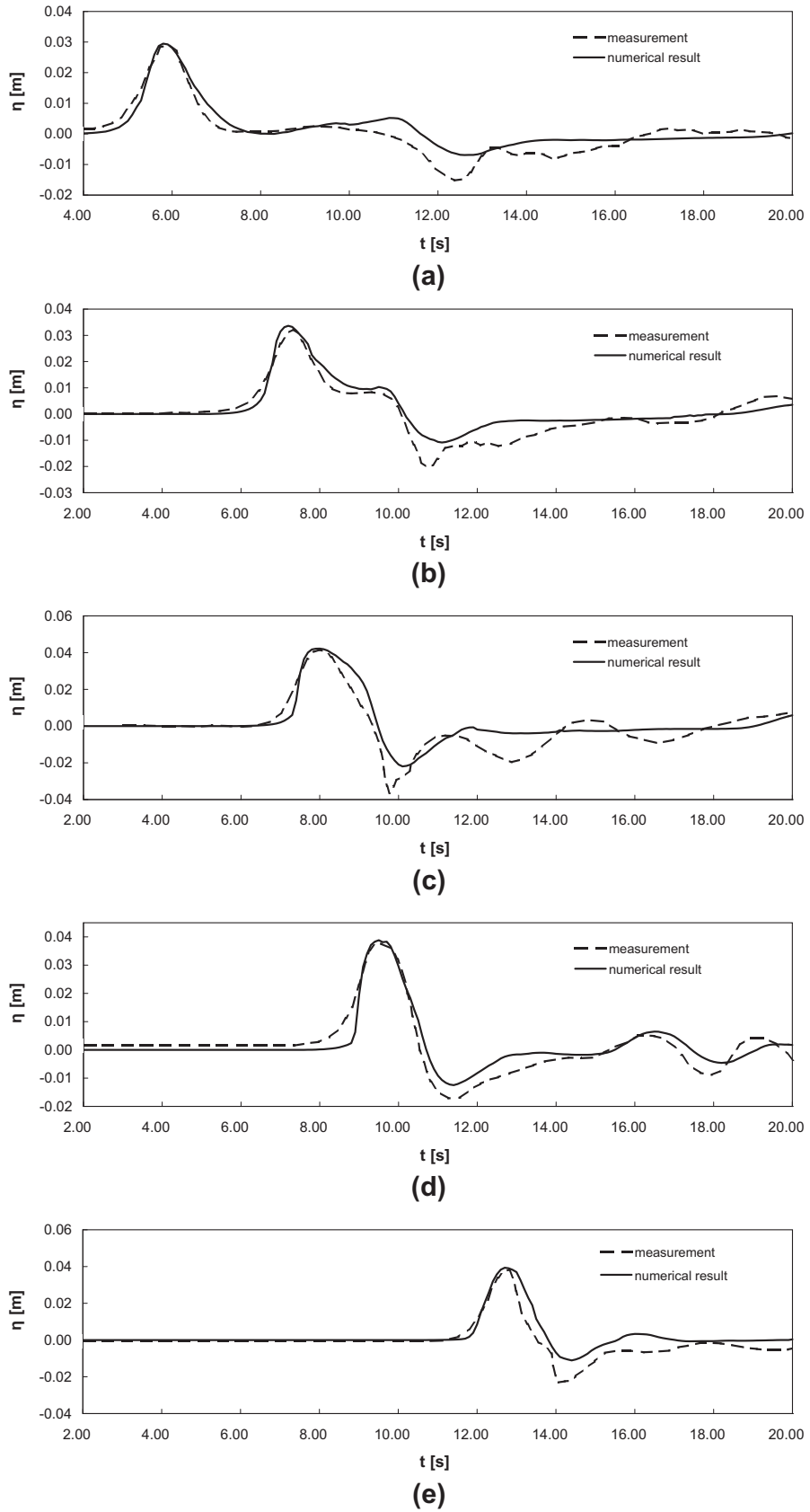
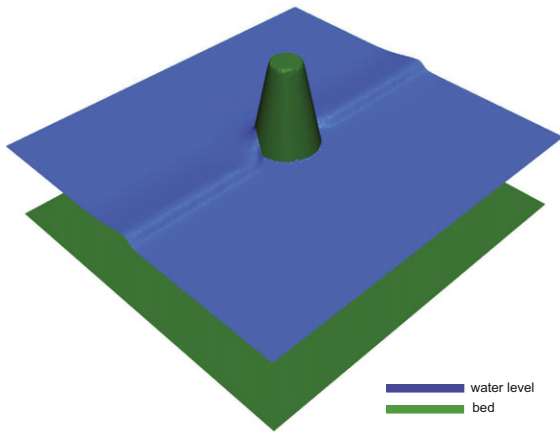
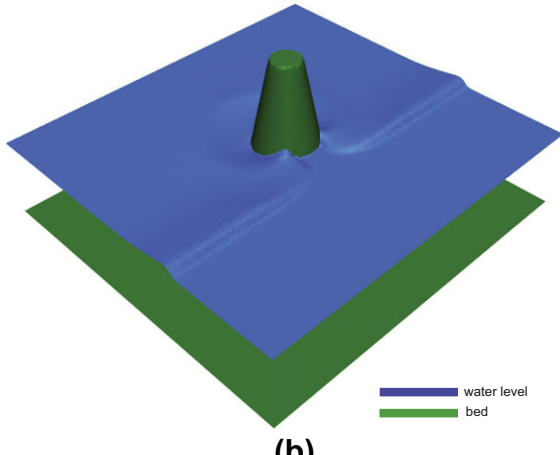


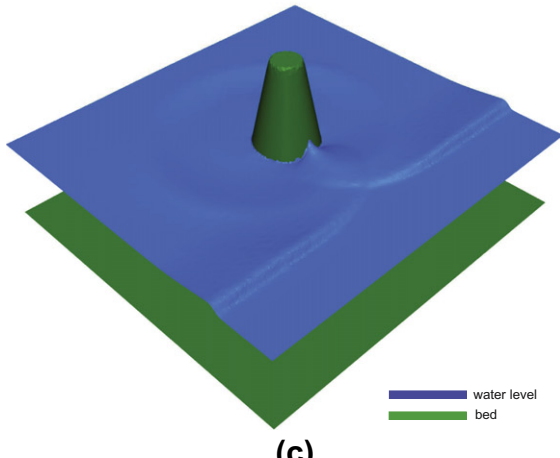
Fig. 33. Solitary wave run-up on a conical island: simulated and measured water levels at WG 3, 6, 9, 16, 22.



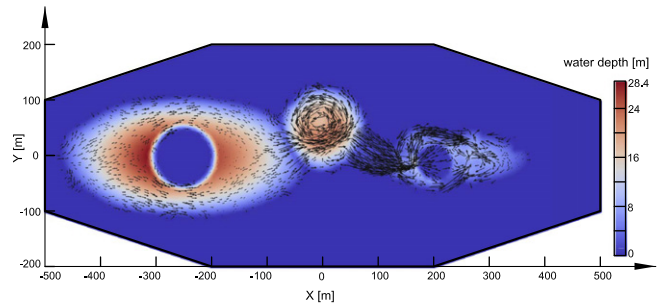
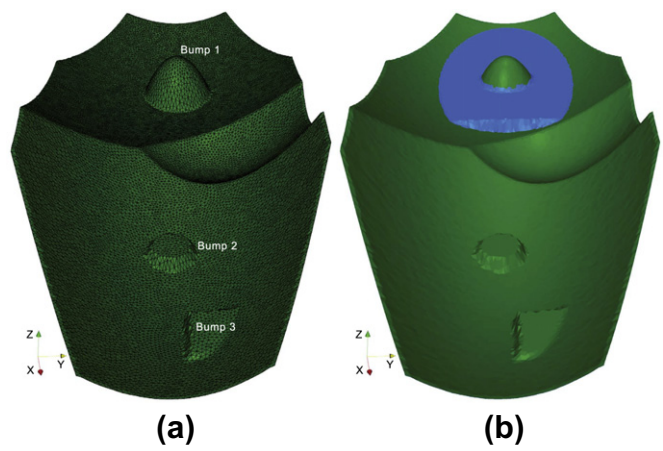
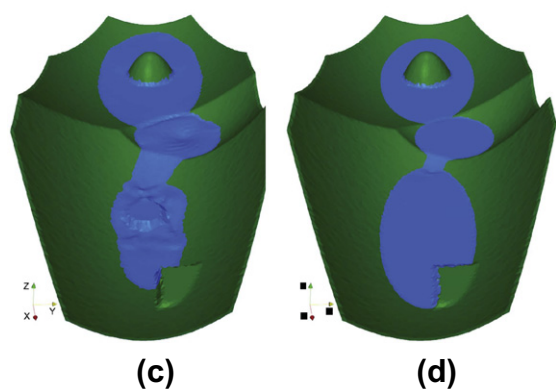
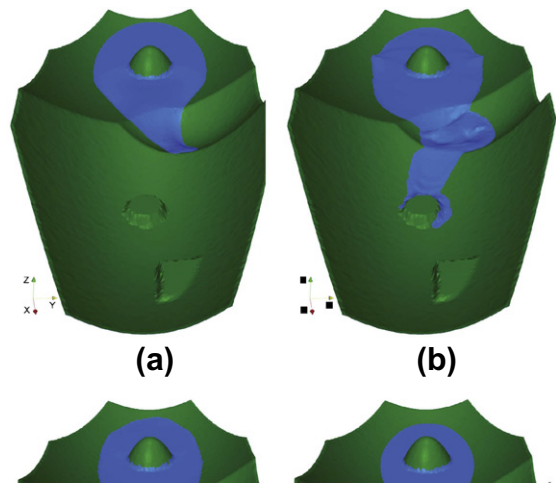
(a)



(b)



(c)

**Fig. 35.** Flow involving wetting and drying over complex bed: computational domain and the computed flow field at $t = 100$ s.**Fig. 36.** Flow involving wetting and drying over complex bed: (a) topography and grid, (b) initial conditions.**Fig. 37.** Flow involving wetting and drying over complex bed: computed free water surface at (a) $t = 10$ s, (b) $t = 40$ s, (c) $t = 100$ s, (d) $t = 500$ s.**Fig. 34.** Simulated solitary wave run-up on a conical island at: (a) $t = 9$ s, (b) $t = 11$ s, (c) $t = 13$ s.

- A robust adaptive method is devised to select an appropriate scheme to extrapolate the values of flow variables at the midpoint of the considered edge, so as to prevent the numerical instabilities caused by the MUSCL reconstruction in the area with varying thin flow over complex bed.
- Based on the Audusse's treatment for the slope source terms (Eq. (38)), an efficient one, which can preserve the C-property for the cells with wet-dry interfaces, is developed for unstructured grids.

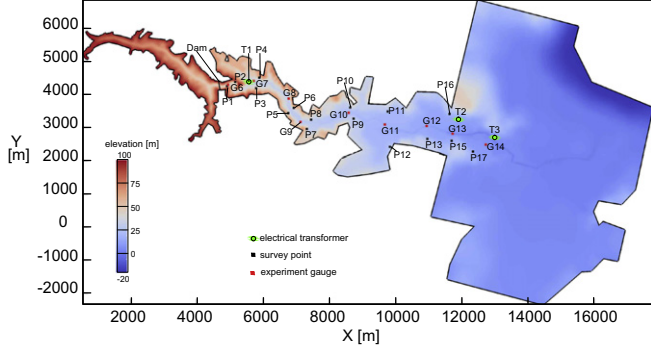


Fig. 38. Malpasset dam-break: topography and locations of electrical transformers T, survey points P and experimental gauges G [35].

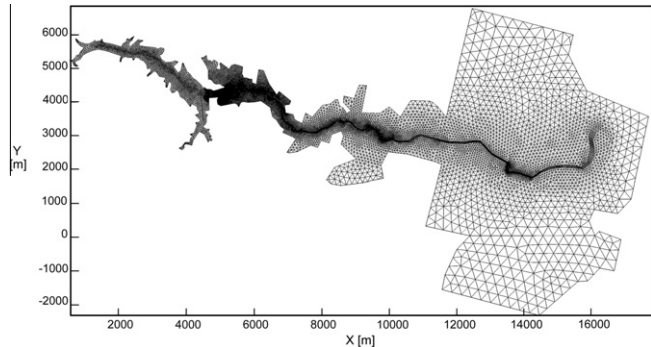


Fig. 39. Malpasset dam-break: computational domain and unstructured grid [91].

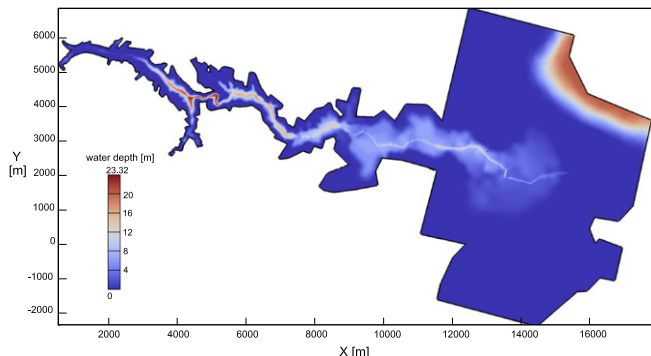


Fig. 40. Malpasset dam-break: predicted inundation map at $t = 2000$ s.

With the new adaptive method together with the proposed slope source term treatment, the present model is applied to simulate several theoretical benchmark tests, several laboratory experiments and a real life dam-break event. The numerical solutions agree quite well with analytical solutions, with alternative numerical solutions and with experiment and field measurements. Besides, unphysical high velocities and negative water depths are successfully avoided. These results indicate that the present model is able to handle the occurrence of wetting and drying, to cope with arbitrary topography, to achieve good convergence to steady stage and to preserve the C-property as well as the mass conservation. In addition, as demonstrated in test cases, the accuracy of the proposed slope source term treatment is nearly the same as that of the Audusse's one [47], but the former is more efficient. To sum up, the present model is accurate, robust and efficient for simulating complex flows over complex beds in complex domains, on unstructured grids.

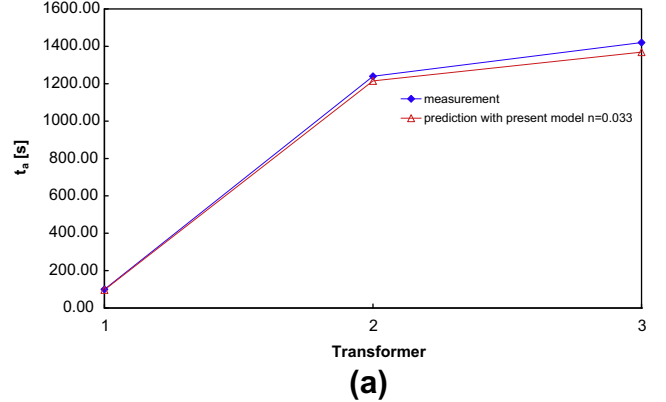


Fig. 41. Malpasset dam-break: comparison between numerical results and survey: (a) arrival times (t_a) at three electrical transformers, (b) maximum water levels (η_{max}) at survey points.

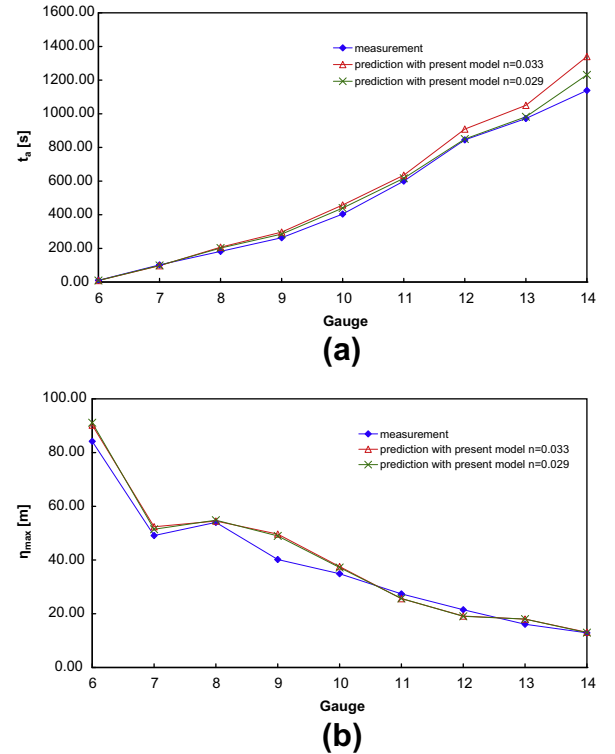


Fig. 42. Malpasset dam-break: comparison between numerical results and experimental measurements at experimental gauges: (a) arrival times (t_a), (b) maximum water levels (η_{max}).

Acknowledgments

China Scholarship Council who supports this research is gratefully acknowledged. The authors also appreciate the three anonymous reviewers especially the first one for the invaluable comments and suggestions, which play an important role to improve this paper.

Appendix A. Proof of the same modified water depths as those in [35]

The water depth at the left hand side of the cell edge under consideration can be modified from Eq. (16) in [35] as

$$\begin{aligned} h_M^L &= \eta_M^L - \min [\eta_M^L, \max (z_{bM}^L, z_{bM}^R)] \\ &= \max [0, \eta_M^L - \max (z_{bM}^L, z_{bM}^R)]. \end{aligned} \quad (81)$$

The water depth at the right hand side of this cell edge can also be modified from the same equation as

$$\begin{aligned} h_M^R &= \max (0, \eta_M^R - \min [\eta_M^R, \max (z_{bM}^L, z_{bM}^R)]) \\ &\quad - \max (0, z_{bM}^R - \min [\eta_M^R, \max (z_{bM}^L, z_{bM}^R)]) \end{aligned} \quad (82)$$

Case 1: if $\eta_M^L \geq \max (z_{bM}^L, z_{bM}^R)$ and $z_{bM}^L \geq z_{bM}^R$, Eq. (82) becomes

$$\begin{aligned} h_M^R &= \max [0, \eta_M^R - \max (z_{bM}^L, z_{bM}^R)] \\ &\quad - \max (0, z_{bM}^R - z_{bM}^L) \\ &= \max [0, \eta_M^R - \max (z_{bM}^L, z_{bM}^R)]; \end{aligned} \quad (83)$$

Case 2: if $\eta_M^L \geq \max (z_{bM}^L, z_{bM}^R)$ and $z_{bM}^L < z_{bM}^R$, Eq. (82) becomes

$$\begin{aligned} h_M^R &= \max [0, \eta_M^R - \max (z_{bM}^L, z_{bM}^R)] \\ &\quad - \max (0, z_{bM}^R - z_{bM}^L) \\ &= \max [0, \eta_M^R - \max (z_{bM}^L, z_{bM}^R)]; \end{aligned} \quad (84)$$

Case 3: if $\eta_M^L < \max (z_{bM}^L, z_{bM}^R)$. In this case, since $\eta_M^L \geq z_{bM}^L$, to satisfy $\eta_M^L < \max (z_{bM}^L, z_{bM}^R)$, z_{bM}^R must be higher than η_M^L and z_{bM}^L . As a result

$$\begin{aligned} h_M^R &= \max [0, \eta_M^R - \eta_M^L] - \max (0, z_{bM}^R - \eta_M^L) \\ &= \eta_M^R - z_{bM}^R = \max [0, \eta_M^R - \max (z_{bM}^L, z_{bM}^R)]; \end{aligned} \quad (85)$$

Evidently, the water depths obtained from Eq. (16) in [35] and Eq. (25) in this work are the same. But the latter is slightly simpler than the former.

References

- [1] K. Anastasiou, C.T. Chan, Solution of the 2D shallow water equations using the finite volume method on unstructured grids, *International Journal for Numerical Methods in Fluids* 24 (1997) 1225–1245.
- [2] S. Chippada, C.N. Dawson, M.L. Martinez, M.F. Wheeler, A Godunov-type finite volume method for the system of shallow water equations, *Computer Methods in Applied Mechanics and Engineering* 151 (1998) 105–129.
- [3] T.H. Yoon, F. ASCE, S.-K. Kang, Finite volume model for two-dimensional shallow water flows on unstructured grids, *Journal of Hydraulic Engineering* 130 (2004) 678–688.
- [4] Q. Liang, A.G. Borthwick, Adaptive quadtree simulation of shallow flows with wet-dry fronts over complex topography, *Computers & Fluids* 38 (2009) 221–234.
- [5] Q. Liang, F. Marche, Numerical resolution of well-balanced shallow water equations with complex source terms, *Advances in Water Resources* 32 (2009) 873–884.
- [6] Q. Liang, Flood simulation using a well-balanced shallow flow model, *Journal of Hydraulic Engineering* 136 (2010) 669–675.
- [7] Y. Wang, Q. Liang, G. Kesserwani, J.W. Hall, A 2D shallow flow model for practical dam-break simulations, *Journal of Hydraulic Research* 49 (2011) 307–316.
- [8] S.F. Bradford, B.F. Sanders, Finite-volume model for shallow-water flooding of arbitrary topography, *Journal of Hydraulic Engineering* 128 (2002) 289–298.
- [9] S.F. Bradford, B.F. Sanders, Performance of high-resolution, nonlevel bed, shallow-water models, *Journal of Hydraulic Engineering* 131 (2005) 1073–1081.
- [10] L. Begnudelli, B.F. Sanders, Unstructured grid finite volume algorithm for shallow water flow and scalar transport with wetting and drying, *Journal of Hydraulic Engineering* 132 (2006) 371–384.
- [11] L. Begnudelli, B.F. Sanders, Conservative wetting and drying methodology for quadrilateral grid finite-volume models, *Journal of Hydraulic Engineering* 133 (2007) 312–322.
- [12] L. Begnudelli, B.F. Sanders, S.F. Bradford, Adaptive Godunov-based model for flood simulation, *Journal of Hydraulic Engineering* 134 (2008) 714–725.
- [13] B.F. Sanders, J.E. Schubert, R.L. Detwiler, ParBreZo: a parallel, unstructured grid, Godunov-type, shallownext term–previous termwaternext term code for high-resolution flood inundation modeling at the regional scale, *Advances in Water Resources* 33 (2010) 1456–1467.
- [14] L. Song, J. Zhou, Q. Li, X. Yang, Y. Zhang, An unstructured finite volume model for dam-break floods with wet/dry fronts over complex topography, *International Journal for Numerical Methods in Fluids* 67 (2011) 960–980.
- [15] L. Song, J. Zhou, J. Guo, Q. Zou, Y. Liu, A robust well-balanced finite volume model for shallow water flows with wetting and drying over irregular terrain, *Advances in Water Resources* 34 (2011) 915–932.
- [16] F. Simons, T. Busse, J. Hou, K. Notay, R. Hinkelmann, A robust and efficient solver for the shallow water equations and its application to a complex natural hydrosystem, in: *Proceedings of the 34th IAHR Congress*, Brisbane, Australia, 2011, pp. 4276–4283.
- [17] A.I. Delis, M. Kazolea, N.A. Kampanis, A robust high-resolution finite volume scheme for the simulation of long waves over complex domains, *International Journal for Numerical Methods in Fluids* 56 (2008) 419–452.
- [18] A.I. Delis, I.K. Nikолос, M. Kazolea, Performance and comparison of cell-centered and node-centered unstructured finite volume discretizations for shallow water free surface flows, *Archives of Computational Methods in Engineering* 18 (2011) 57–118.
- [19] A.I. Delis, I.K. Nikолос, A novel multidimensional solution reconstruction and edge-based limiting procedure for unstructured cell-centered finite volumes with application to shallow water dynamics, *International Journal for Numerical Methods in Fluids* 71 (2013) 584–633.
- [20] J.M. Gallardo, C. Partis, M. Castro, On a well-balanced high-order finite volume scheme for shallow water equations with topography and dry areas, *Journal of Computational Physics* 227 (2007) 574–601.
- [21] D.L. George, Adaptive finite volume methods with well-balanced Riemann solvers for modeling floods in rugged terrain: application to the Malpasset dam-break flood (France, 1959), *International Journal for Numerical Methods in Fluids* 66 (2010) 1000–1018.
- [22] Y. Loukili, A. Soulaimani, Numerical tracking of shallow water waves by the unstructured finite volume WAF approximation, *International Journal for Computational Methods in Engineering Science and Mechanics* 8 (2007) 1–14.
- [23] J. Murillo, P. Garcia-Navarro, J. Burguete, P. Brufau, The influence of source terms on stability, accuracy and conservation in two-dimensional shallow flow simulation using triangular finite volumes, *International Journal for Numerical Methods in Fluids* 54 (2007) 543–590.
- [24] Z.D. Skoula, A.G.L. Borthwick, C.I. Moutzouris, Godunov-type solution of the shallow water equations on adaptive unstructured triangular grids, *International Journal of Computational Fluid Dynamics* 20 (2006) 621–636.
- [25] E.F. Toro, *Riemann Solvers and Numerical Methods for Fluid Dynamics: A Practical Introduction*, third ed., Springer-Verlag, Berlin Heidelberg, 2009.
- [26] J.G. Zhou, D.M. Causon, C.G. Mingham, D.M. Ingram, The surface gradient method for the treatment of source terms in the shallow-water equations, *Journal of Computational Physics* 168 (2001) 1–25.
- [27] J.G. Zhou, D.M. Causon, C.G. Mingham, D.M. Ingram, Numerical prediction of dam-break flows in general geometries with complex bed topography, *Journal of Hydraulic Engineering* 130 (2004) 332–340.
- [28] J. Murillo, P. Garcia-Navarro, J. Burguete, P. Brufau, A conservative 2D model of inundation flow with solute transport over dry bed, *International Journal for Numerical Methods in Fluids* 52 (2006) 1059–1092.
- [29] J. Murillo, P. Garcia-Navarro, J. Burguete, Analysis of a second-order upwind method for the simulation of solute transport in 2D shallow water flow, *International Journal for Numerical Methods in Fluids* 56 (2008) 661–686.
- [30] J. Murillo, P. Garcia-Navarro, J. Burguete, Conservative numerical simulation of multi-component transport in two-dimensional unsteady shallow water flow, *Journal of Computational Physics* 228 (2009) 5539–5573.
- [31] J. Murillo, P. Garcia-Navarro, Improved Riemann solvers for complex transport in two-dimensional unsteady shallow flow, *Journal of Computational Physics* 230 (2011) 7202–7239.
- [32] F. Benkhaldoun, S. Sahmim, M. Seaid, A two-dimensional finite volume morphodynamic model on unstructured triangular grids, *International Journal for Numerical Methods in Fluids* 63 (2010) 1296–1327.
- [33] F. Benkhaldoun, I. Elmahi, M. Seaid, A new finite volume method for flux-gradient and source-term balancing in shallow water equations, *Computer Methods in Applied Mechanics and Engineering* (2010) 3324–3335.
- [34] J.-M. Zokagoa, A. Soulaimani, Modeling of wetting-drying transitions in free surface flows over complex topographies, *Computer Methods in Applied Mechanics and Engineering* 199 (2010) 2281–2304.
- [35] J. Hou, F. Simons, R. Hinkelmann, A 2D well-balanced shallow flow model for unstructured grids with novel slope source treatment, *Advances in Water Resources* 52 (2013) 107–131.

- [36] J.M. Greenberg, A.Y. Leroux, A well-balanced scheme for the numerical processing of source terms in hyperbolic equations, *SIAM Journal on Numerical Analysis* 33 (1996) 1–16.
- [37] A. Bermudez, M.E. Vazquez, Upwind methods for hyperbolic conservation laws with source terms, *Computers & Fluids* 23 (1994) 1049–1071.
- [38] M.E. Hubbard, Multidimensional slope limiters for MUSCL-type finite volume schemes on unstructured grids, *Journal of Computational Physics* 155 (1999) 54–74.
- [39] I. Nikолос, A. Delis, An unstructured node-centered finite volume scheme for shallow water flows with wet/dry fronts over complex topography, *Computer Methods in Applied Mechanics and Engineering* 198 (2009) 3723–3750.
- [40] J. Xia, R.A. Falconer, B. Lin, G. Tan, Modeling flood routing on initially dry beds with the refined treatment of wetting and drying, *International Journal of River Basin Management* 8 (2010) 225–243.
- [41] F.J.M. Simões, Finite volume model for two-dimensional shallow environmental flow, *Journal of Hydraulic Engineering* 137 (2011) 173–182.
- [42] B. van Leer, Towards the ultimate conservative difference scheme. V. A second-order sequel to Godunov's method, *Journal of Computational Physics* 32 (1979) 101–136.
- [43] P. Jawahar, H. Kamath, A high-resolution procedure for Euler and Navier–Stokes computations on unstructured grids, *Journal of Computational Physics* 164 (2000) 165–203.
- [44] F. Benkhaldoun, I. Elmahi, M. Seaid, Well-balanced finite volume schemes for pollutant transport by shallow water equations on unstructured meshes, *Journal of Computational Physics* 226 (2007) 180–203.
- [45] A. Canestrelli, S. Fagherazzi, S. Lanzoni, A mass-conservative centered finite volume model for solving two-dimensional two-layer shallow water equations for fluid mud propagation over varying topography and dry areas, *Advances in Water Resources* 40 (2012) 54–70.
- [46] E. Audusse, F. Bouchut, M.-O. Bristeau, R. Klein, B. Perthame, A fast and stable well-balanced scheme with hydrostatic reconstruction for shallow water flows, *SIAM Journal on Scientific Computing* 25 (2004) 2050–2065.
- [47] E. Audusse, M.O. Bristeau, A well-balanced positivity preserving second-order scheme for shallow water flows on unstructured meshes, *Journal of Computational Physics* 206 (2005) 311–333.
- [48] Y. Xing, C.-W. Shu, High-order finite volume WENO schemes for the shallow water equations with dry states, *Advances in Water Resources* 34 (2011) 1026–1038.
- [49] A. Canestrelli, M. Dumbser, A. Siviglia, E.F. Toro, Well-balanced high-order centered schemes on unstructured meshes for shallow water equations with fixed and mobile bed, *Advances in Water Resources* 33 (2010) 291–303.
- [50] J.H. Pu, N.-S. Cheng, S.K. Tan, S. Shao, Source term treatment of SWEs using surface gradient upwind method, *Journal of Hydraulic Research* 50 (2012) 145–153.
- [51] V. Caleffi, A. Valiani, Well-balanced bottom discontinuities treatment for high-order shallow water equations WENO scheme, *Journal of Engineering Mechanics* 135 (2009) 684–696.
- [52] V. Caleffi, A new well-balanced hermite weighted essentially non-oscillatory scheme for shallow water equations, *International Journal for Numerical Methods in Fluids* 67 (2011) 1135–1159.
- [53] M.E. Hubbard, Garcia-Navarro, Flux difference splitting and the balancing of source terms and flux gradients, *Journal of Computational Physics* 165 (2000) 89–125.
- [54] P. Brufau, M.E.V. Cendón, P. García-Navarro, A numerical model for the flooding and drying of irregular domains, *International Journal for Numerical Methods in Fluids* 39 (2002) 247–275.
- [55] P. Brufau, P. García-Navarro, M.E. Vázquez-Cendón, Zero mass error using unsteady wetting-drying conditions in shallow flows over dry irregular topography, *International Journal for Numerical Methods in Fluids* 45 (2004) 1047–1082.
- [56] M. Castro, A.F. Ferreiro, J. García-Rodríguez, J. González-Vida, J. Macfas, C. ParTs, M.E. Vázquez-Cendón, The numerical treatment of wet/dry fronts in shallow flows: application to one-layer and two-layer systems, *Mathematical and Computer Modeling* 42 (2005) 419–439.
- [57] L. Cea, J. Puertas, Marfa-Elena, Vázquez-Cendón, Depth averaged modeling of turbulent shallow water flow with wet-dry fronts, *Archives of Computational Methods in Engineering* 14 (2007) 303–341.
- [58] M. Ricchiuto, A. Bollermann, Accuracy of stabilized residual distribution for shallow water flows including dry beds, in: E. Tadmor, J. Liu, A. Tzavaras (Eds.), *Hyperbolic Problems: Theory, Numerics and Applications*, volume 67 of *Proceedings of Symposia in Applied Mathematics*, 2009.
- [59] V. Casulli, A high-resolution wetting and drying algorithm for free-surface hydrodynamics, *International Journal for Numerical Methods in Fluids* 60 (2009) 391–408.
- [60] F. Marche, P. Bonneton, P. Fabrie, N. Seguin, Evaluation of well-balanced bore-capturing schemes for 2D wetting and drying processes, *International Journal for Numerical Methods in Fluids* 53 (2007) 867–894.
- [61] P. Sivakumar, D. Hyams, L. Taylor, W. Briley, A primitive-variable Riemann method for solution of the shallow water equations with wetting and drying, *Journal of Computational Physics* 228 (2009) 7452–7472.
- [62] A. Kurganov, G. Petrova, A second-order well-balanced positivity preserving central-upwind scheme for the Saint-Venant system, *Communications in Mathematical Sciences* 5 (2007) 133–160.
- [63] S. Bryson, Y. Epshteyn, A. Kurganov, G. Petrova, Well-balanced positivity preserving central-upwind scheme on triangular grids for the Saint-Venant system, *ESAIM: Mathematical Modeling and Numerical Analysis* 45 (2010) 423–446.
- [64] V. Venkatakrishnan, Convergence to steady state solutions of the Euler equations on unstructured grids with limiters, *Journal of Computational Physics* 118 (1995) 120–130.
- [65] E. Toro, M. Spruce, W. Speares, Restoration of the contact surface in the HLL-Riemann solver, *Shock Waves* 4 (1994) 25–34 (1994).
- [66] C. Michalaki, C. Ollivier-Gooch, Accuracy preserving limiter for the high-order accurate solution of the Euler equations, *Journal of Computational Physics* 228 (2009) 8693–8711.
- [67] J.S. Park, S.-H. Yoon, C. Kim, Multi-dimensional limiting process for hyperbolic conservation laws on unstructured grids, *Journal of Computational Physics* 229 (2010) 788–812.
- [68] W.C. Thacker, Some exact solutions to the nonlinear shallow-water wave equations, *Journal of Fluid Mechanics* 107 (1981) 499–508.
- [69] L. Fraccarollo, E.F. Toro, Experimental and numerical assessment of the shallow water model for two-dimensional dam-break type problems, *Journal of Hydraulic Research* 33 (1995) 843–863.
- [70] E. Toro, *Shock-Capturing Methods for Free-Surface Shallow Flow*, John Wiley, 2001.
- [71] A. Harten, P.D. Lax, B. van Leer, On upstream differencing and Godunov-type schemes for hyperbolic conservation laws, *SIAM Review* 25 (1983) 35–61.
- [72] T.R. Bussing, E.M. Murman, Finite-volume method for the calculation of compressible chemically reacting flows, *AIAA Journal* 26 (1988) 1070–1078.
- [73] S.N. Kuiry, K. Pramanik, D. Sen, Finite volume model for shallow water equations with improved treatment of source terms, *Journal of Hydraulic Engineering* 134 (2008) 231–242.
- [74] M. Sun, K. Takayama, Error localization in solution-adaptive grid methods, *Journal of Computational Physics* 190 (2003) 346–350.
- [75] A. Valiani, L. Begnudelli, Divergence form for bed slope source term in shallow water equations, *Journal of Hydraulic Engineering* 132 (2006) 652–665.
- [76] M. Morris, CADAM: Concerted Action on Dambreak Modeling-Final report, Report SR 571, HR Wallingford, England.
- [77] J.G. Zhou, D.M. Causon, D.M. Ingram, C.G. Mingham, Numerical solutions of the shallow water equations with discontinuous bed topography, *International Journal for Numerical Methods in Fluids* 38 (2002) 769–788.
- [78] IMPACT, EC Contract EVG1-CT-2001-00037. Investigation of Extreme Flood Processes and Uncertainties, 2004, www.impact-project.net.
- [79] S.S. Frazpo, Experiments of dam-break wave over a triangular bottom sill, *Journal of Hydraulic Research* 45 (2007) 19–26.
- [80] M. Ricchiuto, A. Bollermann, Stabilized residual distribution for shallow water simulations, *Journal of Computational Physics* 228 (2009) 1071–1115.
- [81] B.F. Sanders, Integration of a shallow water model with a local time step, *Journal of Hydraulic Research* 46 (2008) 466–475.
- [82] S. Bunya, E.J. Kubatko, J.J. Westerink, C. Dawson, A wetting and drying treatment for the Runge–Kutta discontinuous Galerkin solution to the shallow water equations, *Computer Methods in Applied Mechanics and Engineering* 198 (2009) 1548–1562.
- [83] H.-J. Kim, J.W. Lee, Y.-S. Cho, Numerical simulation of shallow-water flow using a modified Cartesian cut-cell approach, *Journal of Engineering Mechanics* 136 (2010) 399–404.
- [84] M. Briggs, C. Synolakis, G. Harkins, D. Green, Laboratory experiments of tsunami runup on a circular island, *Pure and Applied Geophysics* 144 (1995) 569–593.
- [85] V.V. Titov, C.E. Synolakis, Modeling of breaking and nonbreaking long-wave evolution and runup using VTCS-2, *Journal of Waterway, Port, Coastal, and Ocean Engineering* 121 (1995) 308–316.
- [86] V.V. Titov, C.E. Synolakis, Numerical modeling of tidal wave runup, *Journal of Waterway, Port, Coastal, and Ocean Engineering* 124 (1998) 157–161.
- [87] P.J. Lynett, T.-R. Wu, P.L.F. Liu, Modeling wave runup with depth-integrated equations, *Coastal Engineering* 46 (2002) 89–107.
- [88] M.E. Hubbard, N. Dodd, A 2D numerical model of wave run-up and overtopping, *Coastal Engineering* 47 (2002) 1–26.
- [89] B.H. Choi, D.C. Kim, E. Pelinovsky, S.B. Woo, Three-dimensional simulation of tsunami run-up around conical island, *Coastal Engineering* 54 (2007) 618–629.
- [90] P.L.F. Liu, Y.-S. Cho, M.J. Briggs, U. Kanoglu, C.E. Synolakis, Runup of solitary wave on a circular island, *Journal of Fluid Mechanics* 302 (1995) 259–285.
- [91] N. Goutal, The malpasset dam failure – an overview and test case definition, in: *Proceeding of the 4th CADAM Meeting*, Zaragoza, Spain, 1999.
- [92] A. Valiani, V. Caleffi, A. Zanni, Case study: malpasset dam-break simulation using a two-dimensional finite volume method, *Journal of Hydraulic Engineering* 128 (2002) 460–472.
- [93] D. Liang, B. Lin, R.A. Falconer, A boundary-fitted numerical model for flood routing with shock-capturing capability, *Journal of Hydrology* 332 (2007) 477–486.